

Large eddy simulations of contrail development: Sensitivity to initial and ambient conditions over first twenty minutes

A. D. Naiman,¹ S. K. Lele,¹ and M. Z. Jacobson²

Received 11 February 2011; revised 26 August 2011; accepted 30 August 2011; published 15 November 2011.

[1] A three-dimensional large-eddy simulation with size-resolved ice microphysics was used to model persistent contrails and compute their optical depth and area coverage. Eleven cases were run with various levels of vertical wind shear, aircraft type, relative humidity, ice nuclei effective emission index, and atmospheric stability and were analyzed with respect to their fluid dynamics and ice bulk properties. The effects of these properties on optical depth and contrail width were also compared between cases. Ice properties, optical depths, and contrail widths were consistent with limited observational field studies. For the conditions considered, contrail peak optical depth after twenty minutes simulation time ranged from 0.15 to 0.87, while contrail width ranged from 450 m to over 3 km. Optical depth and contrail width varied most strongly with vertical shear. For a 4-engine aircraft and 130% ambient relative humidity with respect to ice, a moderate shear of 0.005 s^{-1} reduced the peak optical depth by 79% and increased the width by 450% after twenty minutes compared to a zero shear case. In cases with no vertical shear, optical depth was also sensitive to aircraft type, humidity, and effective emission index, but variations in width with these parameters were small. In these cases, larger aircraft, higher humidity, and higher emission indices resulted in optical depths ranging from 20% to 50% larger than baseline cases. Atmospheric stability variations qualitatively changed the fluid dynamical development of the contrail, but differences in optical depth and contrail width were small.

Citation: Naiman, A. D., S. K. Lele, and M. Z. Jacobson (2011), Large eddy simulations of contrail development: Sensitivity to initial and ambient conditions over first twenty minutes, *J. Geophys. Res.*, 116, D21208, doi:10.1029/2011JD015806.

1. Introduction

[2] Assessments of the climate impact of aviation report large uncertainties in quantifying the effect of linear condensation trails (contrails) [e.g., Penner *et al.*, 1999; Forster *et al.*, 2007]. A recent study gives the global radiative forcing of linear contrails as 11.8 (5.4 to 25.6) mWm^{-2} , where these values refer to the best estimate (low range estimate to high range estimate) respectively [Lee *et al.*, 2009]. Compared to the estimate of total aviation radiative forcing of 78 (38 to 139) mWm^{-2} , contrails introduce a significant fraction of the overall uncertainty in the climate impact of aviation. The level of scientific understanding of contrail impacts was assessed as “low” in the same study.

[3] Uncertainty in contrail radiative forcing arises from difficulty in estimating global coverage and optical depth of these anthropogenic clouds. Differentiation between natural cirrus and contrails is difficult in satellite observations, which could otherwise be used to measure these properties. We seek to reduce uncertainties and improve these estimates

by modeling contrail development, including fluid dynamic and microphysical processes, under a variety of ambient atmospheric conditions. These simulations calculate the properties of individual contrails under specific conditions. The results provide data to inform the global models used to estimate climate impacts of aviation.

1.1. Contrail Development

[4] A brief overview of contrail development is helpful for discussing the approaches taken in contrail modeling. Contrails form when jet exhaust, laden with water vapor, volatile particles, and soot from fossil fuel combustion, interacts with the cold ambient atmosphere. When the Schmidt-Appleman criterion is met, water vapor condenses and freezes on condensation nuclei (e.g., emitted soot particles) [Schumann, 1996]. These ice particles may evaporate or sublime quickly if the ambient air is dry, but when the air is supersaturated with respect to ice, they persist and grow. These persistent contrails are the focus of this work.

[5] From a dynamical standpoint, the development of contrails can be split into three distinct regimes: the jet, vortex, and dispersion phases. In the first few seconds after emission, the jet phase, contrail ice forms in the jet exhaust of an aircraft. During this time, velocities from the jet dominate the particle motion. At the same time, vorticity in the wake of the aircraft wing rolls up into a pair of counter-rotating, descending vortices.

¹Department of Aeronautics and Astronautics, Stanford University, Stanford, California, USA.

²Department of Civil and Environmental Engineering, Stanford University, Stanford, California, USA.

[6] As the jet velocity subsides, the vortex pair entrains the exhaust and resident particles. During the vortex phase, the vortices induce downward motion on each other, and the contrail-vortex-wake system descends from the flight level. Some exhaust and contrail particles detrain from this primary wake due to buoyancy, forming a vertical curtain, also called the secondary wake. As the primary wake descends, vortex interactions cause the vortex system to collapse after several minutes and dissipate [Crow, 1970].

[7] Once the organization of the vortex system has collapsed, the contrail enters the dispersion phase. At first, the contrail is dispersed by energy remaining from the vortex system. Vertical oscillations occur due to remaining buoyancy of the hot jet exhaust and descent of the vortex system in the presence of stable stratification. As these motions damp out, the contrail continues to spread due to atmospheric turbulence. Other effects such as radiative heating/cooling and sedimentation of large ice particles may further disperse the contrail.

1.2. Previous Work

[8] Previous numerical simulations of contrails can be categorized based on their fluid dynamic and microphysical models. Two- and three-dimensional codes have been used to simulate contrail dynamics. Bulk microphysical models track a small number of ice parameters on the grid (for example, ice crystal number density and ice mass density) with an assumed size distribution, while binned models calculate the growth of size-resolved particles at much higher cost. A third microphysical formulation tracks ice particle positions with a Lagrangian approach, coupling mass transfer back to the Eulerian fluid grid using source terms.

[9] Early numerical simulation of contrails used two-dimensional models due to computational cost limitations. Gierens [1996] studied the development of contrails starting from the vortex phase with bulk microphysics, while Jensen *et al.* [1998] focused on the effect of radiative heating in the dispersion phase. Gierens and Jensen [1998] conducted a two-part study, with a vortex phase simulation used to initialize a dispersion phase simulation. Three-dimensional LES by Chlond [1998] investigated a range of ambient temperature, humidity, and stability conditions in the dispersion phase. These latter three studies each used a binned microphysics approach to model deposition/sublimation and sedimentation of contrail ice particles.

[10] Lewellen and Lewellen [2001] used a three-dimensional LES with a bulk ice microphysics approach and studied both the vortex and dispersion phase for a range of conditions and aircraft types. Later work by Huebsch and Lewellen [2006] improved on the Lewellen and Lewellen [2001] results with a more detailed binned microphysical model. Paoli *et al.* [2003] and Paoli *et al.* [2004] studied the jet phase and vortex phase with three-dimensional LES. The latter study used a hybrid approach where Lagrangian ice particles were tracked and coupled with a microphysical model. Shirgaonkar and Lele [2007] used a similar hybrid approach in studying the vortex phase.

[11] More recently, Unterstrasser *et al.* [2008] developed a two-dimensional model of the vortex phase that uses a parameterization to account for the dissipation of the vortex system, which is a fundamentally three-dimensional effect.

The results of this study were then used to initialize fields for further two-dimensional simulations of contrails from the end of the vortex phase to several hours into the dispersion phase [Unterstrasser and Gierens, 2010a, 2010b]. Parametric variations in these studies included ambient humidity, temperature, vertical wind shear, and stratification, effective emitted ice crystal number, radiative effects, secondary nucleation effects, and supersaturated layer depth. The model used a new bulk ice microphysics scheme developed to model cirrus clouds [Spichtinger and Gierens, 2009]. Unterstrasser and Sölch [2010] compared results from this bulk microphysical scheme with a Lagrangian tracking approach and found that the bulk scheme adequately captured quantitative trends in ice properties.

[12] Another recent study took a similar two-phase approach, conducting three-dimensional LES first of the vortex and early dispersion phase, then of the later dispersion phase [Paugam *et al.*, 2010]. The focus was on the interaction between vortex dynamics and ambient turbulence. The model used a bulk ice microphysics parameterization similar to Lewellen and Lewellen [2001] and simulated a single aircraft type and atmospheric condition.

1.3. Present Study Approach

[13] In the present study, we simulate the development of contrails from the beginning of the vortex phase, around one second after emission, into the dispersion phase, twenty minutes after emission. We use a three-dimensional large eddy simulation to resolve the energy-carrying scales of the flow. Ice particles are modeled using a Lagrangian tracking scheme and are coupled to the Eulerian fluid simulation through scalar source terms. The fluid phase solver uses an unstructured grid, which allows us to balance computational cost and resolution concerns and achieve a higher spatial resolution than previous studies. The Lagrangian ice tracking scheme also allows balancing of cost and resolution in representing spatial and size distributions of ice particles as the contrail develops.

[14] The simulation duration of twenty minutes was chosen to capture the most important features of linear contrail development. The dynamics that spread the contrail over this time arise due to interactions of the wake of the aircraft and are inherently three-dimensional. By the end of the twenty minute simulations, the contrail is relatively homogeneous in the flight direction, but high fidelity simulation of the early three-dimensional interactions is critical in correctly predicting the development of the contrail up to this time.

[15] Our study includes a parametric variation of conditions including vertical wind shear, aircraft type, ambient humidity, ice nuclei effective emission index, and atmospheric stability. In presenting the results, we focus on the aspects of contrails most relevant to their climate impact. As noted above, much of the uncertainty in estimating this impact is due to a lack of data concerning contrail coverage and optical properties. We therefore present our results by examining sensitivity of contrails with respect to their ice content and geometric extent under the parametric variations.

[16] The major contribution of this work is to simulate both three-dimensional fluid dynamics and size-resolved ice microphysics, and analyze the results with respect to contrail optical depth and area coverage. The parameter space covered

by this work has been explored by the previous studies described above, but none combine three-dimensional fluid dynamics, size-resolved microphysics, and optical depth analysis.

[17] The paper begins with a summary of the computational model in section 2. Section 3 describes the simulation cases, initialization, and run procedure. Section 4 shows results from the simulation cases and comparisons to observational contrail data. Finally, section 6 discusses conclusions from the results and suggests future work.

2. Computational Method

2.1. Fluid Model

[18] The computational domain for the simulations is stationary with respect to the ground, so the computation represents a temporal simulation. The coordinate system is positioned with the x -axis pointing out the right wingtip of the aircraft, the y -axis pointing opposite gravity, and the z -axis pointing opposite the flight direction. The variables p , ρ , θ , and Y represent air pressure, air density, potential temperature, and water vapor density respectively. These are decomposed in the form $f(x, y, z, t) = f_0 + f_y(y) + f'(x, y, z, t)$, where f_0 is a constant reference part, f_y is an altitude varying part, and f' is a perturbation part. The large eddy simulation solves the incompressible Navier-Stokes equations with a Boussinesq approximation for buoyancy forces,

$$\nabla \cdot \mathbf{u} = 0, \quad (1)$$

$$\frac{D\mathbf{u}}{Dt} = -\frac{1}{\rho_0} \nabla p' + \frac{\rho'}{\rho_0} \mathbf{g} + \nu \nabla^2 \mathbf{u} + \nabla \cdot \boldsymbol{\tau}^{sgs}, \quad (2)$$

where $\mathbf{u} = u\mathbf{i} + v\mathbf{j} + w\mathbf{k}$ is the filtered air velocity vector, \mathbf{g} is the gravitational acceleration vector, and ν is the kinematic viscosity of air. The subgrid scale stress tensor, $\boldsymbol{\tau}^{sgs}$, is modeled. The Boussinesq approximation [Spiegel and Veronis, 1960] gives the equation of state,

$$\frac{\rho'}{\rho_0} = \frac{-\theta'}{\theta_0}. \quad (3)$$

[19] Coupled scalar transport equations are solved for potential temperature, θ , water vapor density, Y , and a passive scalar, ϕ ,

$$\frac{D\theta'}{Dt} = -\frac{d\theta_y}{dy} v + \kappa \nabla^2 \theta' + \nabla \cdot \mathbf{q}^{sgs, \theta} + \omega_T, \quad (4)$$

$$\frac{DY'}{Dt} = -\frac{dY_y}{dy} v + D_v \nabla^2 Y' + \nabla \cdot \mathbf{q}^{sgs, Y} + \omega_Y, \quad (5)$$

$$\frac{D\phi}{Dt} = D_v \nabla^2 \phi + \nabla \cdot \mathbf{q}^{sgs, \phi}, \quad (6)$$

where κ is the thermal diffusivity of air and D_v is the diffusivity of water vapor in air. Temperature and water vapor density are prescribed to vary linearly with altitude, so the vertical gradients $d\theta_y/dy$ and dY_y/dy are constants. The subgrid scale stress tensors, \mathbf{q}^{sgs} , are modeled for each scalar

variable. The source terms ω_T and ω_Y couple ice microphysics to the vapor phase through mass exchange of water and latent heat release by ice sublimation/deposition. The terms are related,

$$\rho_0 C_p \omega_T = -\omega_Y L, \quad (7)$$

where C_p is the specific heat of air and L is the latent heat of sublimation of ice. The source term ω_Y is calculated in the ice microphysics model described below.

[20] The simulation code is based on the incompressible version of a generalized unstructured grid LES solver developed at the Center for Turbulence Research at Stanford University. The spatial discretization is a second-order finite volume scheme designed to minimize numerical dissipation and preserve the flow structure. Subgrid scale stresses are modeled using a dynamic Smagorinsky model. Time advancement is by a second-order implicit fractional step method. A detailed description of the algorithms is presented in Mahesh *et al.* [2004] and Ham *et al.* [2007].

2.2. Ice Model

[21] The contrail ice particles are tracked using a Lagrangian approach similar to that described by Paoli *et al.* [2004]. A collection of N_{comp} computational particles is introduced into the flow, each representing N_p physical particles. The location, \mathbf{x}_p , of a computational particle represents the center of mass of these N_p physical particles. The full equations of motion for particles are complex [see, e.g., Maxey and Riley, 1983], but can be simplified for the case of small Stokes number. The Stokes number, $St = \tau_p/t_0$, characterizes the ratio of the particle response time, τ_p , to the characteristic flow timescale, t_0 . Appendix A presents results showing the maximum Stokes number for particles during the simulation. The maximum value below 2×10^{-4} is well within the regime of small Stokes number assumptions.

[22] For small Stokes numbers, the particles follow the carrier fluid pathlines, so their Lagrangian location can be advanced in time,

$$\frac{d\mathbf{x}_p}{dt} = \mathbf{u}(\mathbf{x}_p, t). \quad (8)$$

[23] A third-order Runge-Kutta scheme integrates equation (8) in time using fluid velocities interpolated from the Eulerian grid.

[24] The ice sublimation/deposition model is based on a simple diffusional model given by Kärcher *et al.* [1996]. Ice particles are treated as a spherical nucleus over which ice deposits. The change in radius of a particle, r_p is given by

$$\frac{dr_p^2}{dt} = \frac{2D_v}{\rho_p} \rho G(r_p) (X - X_{sat}), \quad (9)$$

where D_v is the diffusivity of water vapor in air, ρ_p is the particle density, $G(r_p)$ is the diffusional growth factor, X is the local water vapor volume mixing ratio, X_{sat} is the local saturation water vapor volume mixing ratio, and ρ is the air density. The diffusional growth factor is given by

$$G(r_p) = \left(\frac{1}{1 + Kn} + \frac{4Kn}{3\alpha} \right)^{-1}, \quad (10)$$

where Kn is the Knudsen number and α is the deposition coefficient, taken as 1. The local water vapor volume mixing ratio, X , is given by

$$X = \frac{(1 + \epsilon)Y}{1 + \epsilon Y}, \quad (11)$$

where $\theta = M_{\text{air}}/M_{\text{H}_2\text{O}} - 1$ and Y is interpolated to the particle position from the Eulerian grid. The local saturation water vapor volume mixing ratio, X_{sat} , is given by

$$X_{\text{sat}} = \frac{p_{\text{sat}}}{p}, \quad (12)$$

where p is interpolated to the particle position from the Eulerian grid. The local saturation vapor pressure over ice, p_{sat} , is estimated from a *Murphy and Koop* [2005] data fit with an additional factor, K , accounting for the Kelvin effect,

$$p_{\text{sat}} = K \exp(9.550426 - 5723.265/T + 3.53068 \ln(T) - 0.00728332T), \quad (13)$$

where T is the total temperature and the Kelvin effect factor, K , is given by,

$$K = \exp\left(\frac{2\sigma M_{\text{H}_2\text{O}}}{r_p R T \rho_p}\right), \quad (14)$$

where σ is the surface tension of the ice-vapor interface and R is the universal gas constant. Note that due to the Kelvin effect and the assumed ice nucleus radius, $r_{p,\text{min}}$, ice particles that sublimate entirely are unlikely to grow again in the simulation because they will not encounter humid enough conditions. Sensitivity to the choice of $r_{p,\text{min}}$ has not been investigated in this work.

[25] Equation (9) is integrated analytically assuming constant X and $G(r_p)$, equivalent to an Euler explicit step for r_p^2 . Ice sublimation is limited by assuming that the ice nucleus is composed of nonvolatile material, so particle radius reduction is clipped at a minimum radius, $r_{p,\text{min}}$. The source term for water vapor density in equation (5), ω_Y , is calculated by integrating, for each Eulerian control volume, the mass of water deposited to the particles in that volume,

$$\Delta m = \sum \frac{4}{3} \pi \rho_p N_p (r_p^3 - r_{p,\text{old}}^3), \quad (15)$$

where r_p and $r_{p,\text{old}}$ represent the particle radius at the end and beginning of a time step, respectively. This mass is distributed to the nodes of the control volume by an inverse distance-squared weighting and divided by the local node volume, ΔV , to give the source term integrated over the time step (as required by the LES numerical scheme),

$$\omega_Y \Delta t = -\frac{\Delta m}{\Delta V}. \quad (16)$$

2.3. Limitations of the Ice Model

[26] The high number concentration of ice particles present in a contrail necessitates the use of a model to represent size and spatial distributions. The Lagrangian ice

microphysical model used in this work was chosen as an alternative to the bulk and binned models used in some previous contrail studies as noted in section 1.2. Each of these models is subject to limitations that are important to consider when interpreting their results.

[27] The Lagrangian resolution (that is, the number of computational particles tracked) used in our simulations balances between accuracy of the results and computational cost. Throughout the simulations, as the contrail grows in volume and as the Eulerian grid resolution decreases, the number of particles per control volume in the contrail is of order 10. In the denser core, the size distribution is well represented, but in more sparsely populated regions, the model is unable to resolve the size spectrum. Validation cases testing the effect of increasing the Lagrangian resolution are presented in *Naiman* [2011], but cost considerations prevented computation of a converged solution to assess the quantitative errors. It is possible that this limitation may cause considerable uncertainties relative to results using an order of magnitude more computational particles. For comparison, *Unterstrasser and Sölch* [2010] reported that their two-dimensional simulations using Lagrangian particles were converged when 1000 particles per control volume were used.

[28] In addition to this computational limitation, our microphysical model neglects forces on the particles such as drag and gravitational settling, which become more important for larger Stokes numbers. A validation case has been conducted to assess these effects and is presented in Appendix A. Grid-scale diffusion of particles is not included in the model, nor is the effect of sub-grid scale velocity fluctuations, since the fluid velocity, \mathbf{u} , is the LES filtered velocity. The dispersion of the Lagrangian phase is therefore not exactly consistent with the dispersion of the Eulerian phase. The effect of the sub-grid scale model on ice growth and particle spatial distribution has not been investigated in the context of contrails, but has been shown to affect results in other applications (see, e.g., *Shotorban and Mashayek* [2006] or *Pozorski and Apte* [2009]). Future work is planned to address this issue. Analysis of passive Lagrangian and Eulerian tracers showed that their distribution after twenty minutes of simulation time differed by as much as 30% in localized regions. The quantitative effect of these differences has not been assessed.

3. Simulation Description

[29] We present the results of eleven sensitivity cases in section 4. Unless otherwise noted, each case simulation is conducted using the conditions and procedures detailed here.

3.1. Simulation Conditions

[30] Commercial aircraft encounter a wide range of atmospheric conditions during their flights. Aircraft burn much of their fuel at cruise altitudes between 9–12 km [*Wilkerson et al.*, 2010], the range of altitudes at which contrails are most likely to form [*Schumann*, 2005]. We are interested in the subset of conditions at which contrails persist, which is still a large parameter space. We have chosen to focus on important sensitivities, and limit the conditions by simulating all cases under standard atmosphere

Table 1. Key Atmospheric Parameters for the Simulation Cases, Based on Standard Atmosphere Conditions at 10.5 km Altitude

Parameter		Value	
T_0	Reference temperature	219	K
ρ_0	Reference air density	0.38	kg/m ³
p_0	Reference air pressure	2.4×10^4	Pa
ν_{air}	Air kinematic viscosity	3.8×10^{-5}	m ² /s
Pr	Prandtl number	0.70	
Sc	Schmidt number	0.65	

conditions at an altitude of 10.5 km. Some key parameters for this condition are listed in Table 1.

[31] The sensitivity cases vary vertical wind shear magnitude, aircraft size and configuration, ambient relative humidity, ice nuclei effective emission index, and vertical stability. Summaries of the sensitivity cases are listed in Table 2.

3.2. Initial Conditions

[32] For each simulation, a background field of developed, periodic, isotropic, decaying turbulence is generated as suggested by *Rogallo* [1981]. The velocity field is then scaled such that its energy matches the inertial subrange spectra at a peak wave number for a given turbulent dissipation rate, $\epsilon = 1 \times 10^{-4}$ m²/s³. The initial field is isotropic with an integral length scale of approximately 2 spans. For the cases with vertical wind shear, a linearly varying velocity field is also added to the background field.

[33] Each case velocity field is then initialized by adding a two-dimensional vortex-jet wake extruded in the flight direction to the background field. The vortex-jet wake uses idealized Lamb-Oseen vortices and Gaussian jets to define the velocity fields. Schematics of the three different initial fields are shown in Figure 1. Table 3 shows key initial condition parameters that are identical for each of the sensitivity cases. Table 4 gives the parameters used to define the initial fields. The medium 2-engine initial condition field is based on a previously conducted Boeing 767 wake simulation. The parameters for the other cases are based on estimates of typical operating conditions for aircraft of each size. The jet and vortex core locations are defined relative to the aircraft centerline, which is located at $(x, y) = (0, 2.0)$ spans in order to allow for vortex descent in the domain. The

jets are centered at $(\pm\Delta x_j, 2.0 - \Delta y_j)$ spans and the vortices at $(\pm\Delta x_v, 2.0)$ spans.

[34] In addition to the velocity fields, the initial condition fields include a distribution of water vapor, temperature, and a passive jet exhaust scalar. These variables are introduced at the Gaussian jet locations with integrated values in the contrail cross-section as listed in Table 4. The passive scalar has an initial peak value of 1.0.

[35] The final component of each case initial condition is the distribution of ice particles. For each case, the particles are distributed randomly in the domain in proportion to the jet exhaust scalar. The peak concentration is scaled such that the total number of particles $n = N_p \times N_{comp}$ corresponds to a prescribed ice number effective emission index and assumed fuel mass flow rate for each aircraft. Note that ice particles are formed from the products of hydrocarbon combustion downstream of the engine, and so are not actually emitted. The formation of ice nuclei is still an open issue in the literature and is not treated here [*Kärcher and Yu*, 2009]. Particle radii are initially monodisperse and small enough that most of the emitted water is in vapor form. Our approach is to allow the initial particle size distribution to form naturally due to competition between ice nuclei spatially distributed in the jet exhaust, rather than prescribing an initial size distribution with all of the emitted water as ice.

[36] Note that the initial condition chosen for these simulations is simplified from a realistic aircraft wake, and could affect the spatial distribution of ice in the contrail as it develops. For example, the initial distribution of ice may affect how it is partitioned between the primary and secondary wake. This sensitivity has not been assessed.

3.3. Numerical Considerations and Running Procedure

[37] Periodic boundary conditions are used for all of the simulations. The typical periodic boundary conditions are modified to allow a step in horizontal velocity at the top and bottom of the domain for the vertical wind shear cases. The unstructured grid capabilities of the simulation code are utilized to ensure that the boundary conditions do not influence the flow solutions. Grid resolution is maximized in the center of the domain, where the contrail and vortex wake structure is located. Resolution is decreased outside this central region to allow the boundaries to be placed far from the major flow structures while keeping computational costs

Table 2. Summaries of the Sensitivity Cases

Case	Sensitivity	Aircraft Type ^a	Shear ^b	RHi ^c	N_{bv} ^d	$El_{ice\#}$ ^e
E	Baseline	Medium 2-Engine	0	130%	0.01 s ⁻¹	10 ¹⁵ kg ⁻¹
F	Aircraft Type	Large 4-Engine	0	130%	0.01 s ⁻¹	10 ¹⁵ kg ⁻¹
G	Aircraft Type	Small 2-Engine	0	130%	0.01 s ⁻¹	10 ¹⁵ kg ⁻¹
C	Shear	Medium 2-Engine	0.005 s ⁻¹	130%	0.01 s ⁻¹	10 ¹⁵ kg ⁻¹
H	Shear	Large 4-Engine	0.005 s ⁻¹	130%	0.01 s ⁻¹	10 ¹⁵ kg ⁻¹
L	RHi	Medium 2-Engine	0	120%	0.01 s ⁻¹	10 ¹⁵ kg ⁻¹
M	RHi	Medium 2-Engine	0	110%	0.01 s ⁻¹	10 ¹⁵ kg ⁻¹
E2	Emission Index	Medium 2-Engine	0	130%	0.01 s ⁻¹	10 ¹⁴ kg ⁻¹
M2	Emission Index	Medium 2-Engine	0	110%	0.01 s ⁻¹	10 ¹⁴ kg ⁻¹
E4	Stability	Medium 2-Engine	0	130%	0.0 s ⁻¹	10 ¹⁵ kg ⁻¹
E5	Stability	Medium 2-Engine	0	130%	0.015 s ⁻¹	10 ¹⁵ kg ⁻¹

^aExplanations of the aircraft type initial conditions are given in the text.

^bShear refers to vertical wind shear (du/dy).

^cRHi is the relative humidity with respect to ice.

^d N_{bv} is the Brunt-Väisälä frequency.

^e $El_{ice\#}$ is the ice number effective emission index.

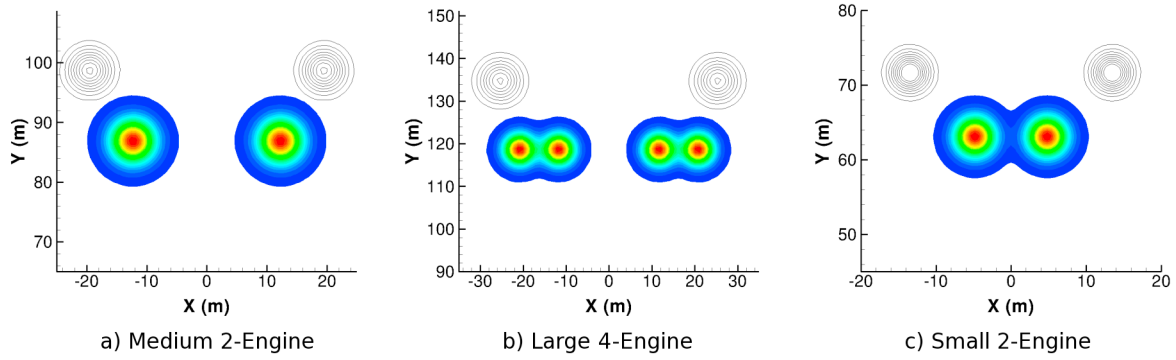


Figure 1. Schematics of the three different aircraft wake initial condition fields. Black and white contours indicate vorticity; colored contours indicate jet exhaust scalar concentration.

low. Grid resolution is uniform in the z – direction at each (x, y) location. A sample grid cross-section from early in the simulation is shown in Figure 2.

[38] During the simulation, the resolution required to capture the relevant flow scales decreases and the cross-sectional area of the contrail increases. A series of six grids is used to capture this change in scales, with results from the end of the simulation on one grid interpolated to the next grid in the series. Table 5 shows a typical progression of grids used for the zero shear cases, from smaller domain/higher resolution to larger domain/lower resolution. As shown there, domain sizes and grid spacings are scaled by the wing span of the aircraft. The shear cases use similar grids, but with the domain expanded in the cross-stream (x) direction to contain the sheared contrail.

[39] In addition to the Eulerian grid resolution, the choice of Lagrangian resolution (that is, the number of computational particles, N_{comp} , to be tracked) is important to resolve particle size distributions within control volumes and account for competition between particles of different sizes. As ice number density and Eulerian grid resolution change throughout the simulation, N_{comp} remains constant, and was chosen to keep the number of computational particles per control volume inside the contrail near 10. Two validation exercises were undertaken to determine that this quantity of computational particles is sufficient [Naiman, 2011].

[40] The simulation code supports variable time stepping, which provides a compromise between temporal accuracy and computational cost. The time step is set by limiting the maximum Courant number, $u\Delta t/\Delta x$, to 1.0 in the domain. Typical time steps for each stage of the simulation are shown in Table 5. At late simulation times, when fluid velocities are lower and grid spacing larger, the time step is limited to $\Delta t = 0.5$ s in order to produce visualization and post-processing data at regular intervals. A typical twenty-minute case required 7500 time steps. Simulations are conducted on supercomputing resources at NCSA and LONI and typically required 25000 cpu-hours (50 hours of wall-clock time on 500 processors) per twenty-minute simulation.

4. Results

[41] Each of the cases described above has been run for twenty minutes of simulation time. In this section, we first

describe results from a baseline case (case E). We then compare the various cases and note the sensitivities to the varied parameters.

[42] The dynamic behavior of contrails has been described previously in the literature, as have sensitivities of dynamics and ice content to aircraft type, ambient humidity, and shear [e.g., Lewellen and Lewellen 2001]. We present this discussion with analysis from our simulations to inform later presentation of contrail width and optical depth sensitivities.

4.1. Baseline Results

[43] As noted in section 1, the development of a contrail can be split into three distinct regimes based on the dominant flow scales: jet, vortex, and dispersion phases. Our simulation focuses on the vortex and dispersion phases. Within the first five seconds of the case E simulation, the jet plumes are entrained by the vortices. The vortices dominate the early flow field, and much of the contrail descends as the primary wake at a rate of approximately 1.7 m/s. A secondary wake forms when a portion of the warm jet exhaust detrains from the primary wake due to its buoyancy producing baroclinic vorticity of opposite sign from the primary wake. The secondary wake appears as a vertical curtain left behind as the primary wake descends. This general development has been described in detail in previous work investigating the distribution of aircraft emissions [Gerz et al., 1998; Holzäpfel et al., 2001]. Here, we focus on the spreading of the contrail material by the vortex dynamics.

[44] This entrainment, descent, and partitioning of the wake can be visualized by examining the fluid dynamic field data from the simulation. Figure 3 shows a sequence of three-dimensional isosurfaces as the vortex-wake system develops over the first several minutes of the simulation. The vortices can be seen in the isosurfaces of vorticity, the levels of which were chosen at each time step to highlight the vortex cores. The outer extent of the contrail material is denoted by an isosurface of the passive scalar that serves as

Table 3. Key Simulation Parameters That Are the Same for All Initial Conditions

Parameter		Value
$r_{p, init}$	Initial particle radius	$0.1 \mu\text{m}$
$r_{p, min}$	Ice nucleus radius	$15 \times 10^{-3} \mu\text{m}$
N_{comp}	Number of computational particles	8×10^6

Table 4. Simulation Parameters for the Idealized Initial Condition Fields

	Parameter	Medium 2-Engine	Large 4-Engine	Small 2-Engine	Units
b	Wing span	47.2	64.5	34.3	m
V_0	Cruise speed	236.9	236.9	233.4	m/s
M_a	Aircraft mass	170×10^3	300×10^3	60×10^3	kg
Γ_0	Initial Circulation	391	646	246	m ² /s
\dot{m}_f	Fuel mass flow	5.8	11.6	2.5	kg/km
$\int \Delta T$	Integrated exhaust heat	457	915	197	Km ²
$\int \Delta Y$	Integrated emitted water	7.25×10^{-3}	14.5×10^{-3}	3.13×10^{-3}	kgH ₂ O/m
r_j	Jet core radius	0.15	0.11	0.15	spans
Δx_j	Jet core location	0.26	0.18, 0.32	0.14	spans
Δy_j	Jet core location	0.16	0.16	0.16	spans
r_v	Vortex core radius	0.07	0.07	0.07	spans
Δx_v	Vortex core location	0.41	0.39	0.39	spans

a tracer of the jet exhaust. The counter-rotating vortices are mostly parallel after one minute, but small perturbations grow as ambient turbulence triggers the Crow instability. As the vortices loop off, they push the contrail out quickly in the spanwise direction, developing a characteristic periodic puffy structure. By $t = 300$ s, the vortex system has become disorganized, and additional spreading of the contrail occurs as the vortices disperse.

[45] The effect of the vortex wake dynamics on the contrail can be visualized by examining flight-direction averaged contours, which give a cross-sectional view. Figure 4 shows contours of relative humidity and ice mass density in the contrail at early times. At $t = 30$ s, the contrail is tightly bound in the descending vortex pair. The interior of the vortex system is near saturation ($RHi = 100\%$) and the ice mass of the contrail is concentrated in the same region. As the vortices descend, the region near saturation extends from the primary wake up into the secondary wake. Since the vortices have linked by $t = 120$ s, the flight-direction is inhomogeneous in the primary wake region, so this region appears to be more supersaturated and contain less ice in the averaged view. By $t = 300$ s, the vortices have dissipated, and the primary wake has spread inhomogeneously in the spanwise direction. The region near saturation still extends up into the secondary wake, and ice mass density is greatest in the same central, vertical curtain.

[46] Kinetic energy from the wake system appears in two forms in the simulation after about $t = 300$ s: remaining energy from the vortex system and vertical oscillation of the wake due to the stable atmospheric environment. As the vortex system dissipates due to chaotic vortex interactions and viscous effects, its energy appears as turbulence in what was the primary descending portion of the wake. This contributes to additional spanwise spreading of the lower portion of the wake at later times.

[47] The vertical oscillation of the wake appears in both the primary (bottom) and secondary (top) portions. Figure 5 shows a slice of the wake that follows the center of the downward puff through the early dispersion phase. Contours of perturbation temperature (which correspond to buoyancy) are plotted for the slice, as well as vectors showing the velocity field tangent to the slice plane. The vertical motion of the primary and secondary portions of the wake can be related to their buoyancy by examining these plots.

[48] The primary wake is initially warmer than ambient air due to entrainment of the warm jet exhaust. Once released from the influence of the descending vortex system, this

exhaust rebounds due to its buoyancy. The velocity vectors in the $t = 240$ s show the strong upward flow that results. By $t = 480$ s, the primary wake exhaust has largely reached an equilibrium position, and residual turbulence is reflected in spanwise spreading until the end of the simulation.

[49] The secondary wake forms when a portion of the warm jet exhaust detrains from the primary wake due to its buoyancy producing baroclinic vorticity of opposite sign from the primary wake. As the secondary wake rises, it overshoots its equilibrium height and rebounds. At $t = 240$ s, the secondary wake has neutral buoyancy, but is still moving upward. Patches of strong negative buoyancy appear by $t = 360$ s. As this fluid reaches an equilibrium position, the top of the wake flattens and spreads in the spanwise direction.

[50] Figure 6 shows contours of relative humidity and ice mass density at later times, corresponding to the dispersion

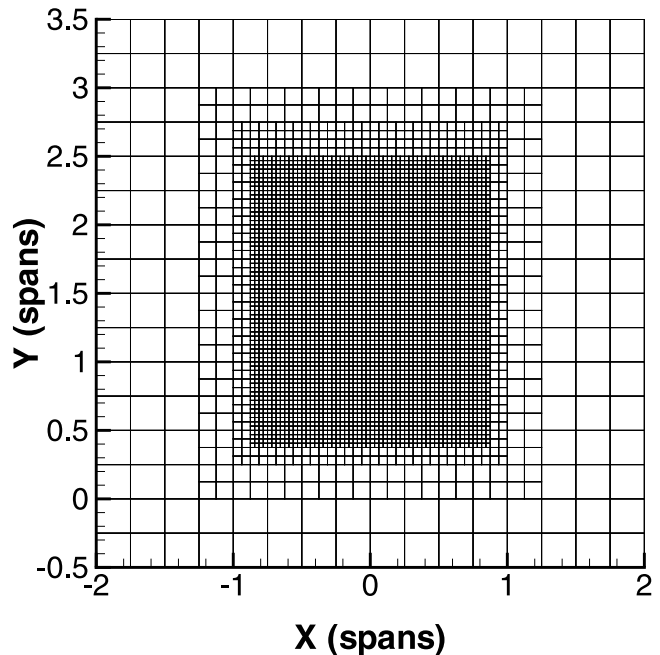


Figure 2. This sample grid cross-section from early in the simulation shows three levels of refinement from the background grid to the central region. The original resolution has been reduced by a factor of four in each direction to show details. The full background grid extends to ± 4 spans in each direction. Grid resolution is uniform in the z -direction at each (x, y) location.

Table 5. Typical Progression of Grids for a Simulation Case^a

	Stage 1	Stage 2	Stage 3	Stage 4	Stage 5	Stage 6	Units
Simulation time	0–30	30–60	60–120	120–300	300–600	600–1200	s
Domain size	$8 \times 8 \times 8$	$8 \times 8 \times 8$	$8 \times 8 \times 8$	$16 \times 16 \times 8$	$24 \times 24 \times 8$	$32 \times 32 \times 8$	b^3
Central resolution	1/128	1/64	1/64	1/32	1/24	1/16	b
Number of nodes	34	18	33	20	17	14	$\times 10^6$
Typical time step	0.02	0.04	0.04	0.25	0.5	0.5	s

^aThe domain size and resolution are scaled by wing span, b , for each aircraft type as shown in Table 4.

phase of the simulation. In this phase, the development of the contrail is dominated by turbulent mixing of the aircraft exhaust plume with ambient air. The motion of the vortex system is no longer organized, but the energy remaining in the primary wake spreads the contrail horizontally. Vertical motions of the contrail are driven by buoyancy effects. As the energy of the aircraft wake dissipates, atmospheric turbulence comes to dominate the mixing of humid ambient air into the contrail. As the contrail spreads from $t = 600$ s to 1200 s, the entrainment of ambient humidity into the contrail is seen in the increase of ice mass density in the central region. The region of near saturation humidity also grows in the averaged view as mixing re-homogenizes the contrail in the flight direction.

[51] The growth of ice in the contrail will be further examined in the following section, as it is sensitive to the parameters varied here. The general behavior of ice growth is the same for all of the cases, and can be seen in the domain-integrated ice size distributions shown in Figure 7. From the initial monodisperse particle size, ice grows very quickly at the beginning of the simulation to a narrow distribution of sizes as the water vapor emitted in the jet exhaust deposits on the particles (Figure 7a). During the

remainder of the vortex phase, humid ambient air is entrained and some larger particles grow, while some smaller particles in the interior of the contrail sublimate due to locally subsaturated conditions. The result is a broadening of the size distribution (Figure 7b). As the vortices dissipate and the contrail enters the dispersion phase, the entrainment of humid air by mixing dominates ice growth, and the distribution moves toward larger particle sizes (Figure 7c).

[52] These features are also reflected in the properties of ice integrated throughout the simulation domain. Figure 8 shows some domain-integrated ice statistics plotted against simulation time. The first, percentage of surviving ice particles, refers to the particles that have not sublimated down to their nucleus. As the contrail develops, available water vapor above saturation is quickly deposited onto ice particles until the interior of the contrail is near saturation. Adiabatic compression warms the primary wake as it descends, reducing its relative humidity and causing some ice to sublimate (see Figure 9). As smaller particles encounter locally subsaturated conditions in the contrail, they may reach a size too small to grow again without much higher supersaturations than are present in the simulation (i.e., due to the Kelvin effect). For this reason, the number of surviving particles decreases

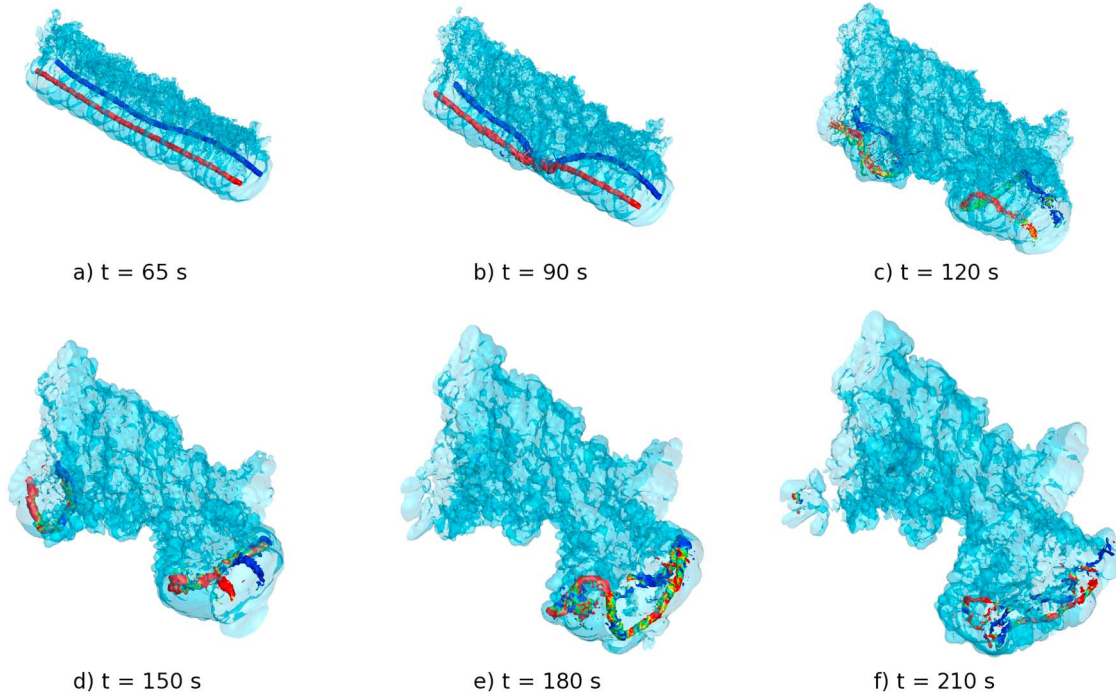


Figure 3. Time sequence of the vortex wake breakdown and contrail, from 65 to 210 seconds after emission, for case E. The opaque isosurfaces show vorticity magnitude, colored by streamwise vorticity. The transparent isosurface shows the outer extent of the passive exhaust scalar.

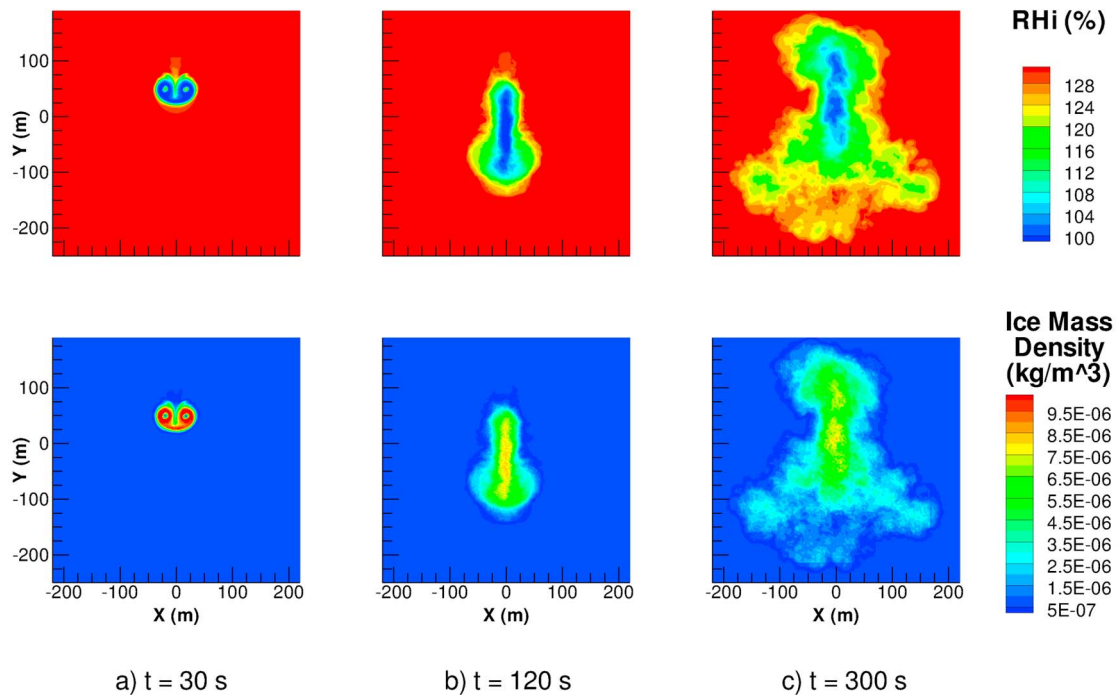


Figure 4. Flight-direction averaged contours of relative humidity with respect to (top) ice and (bottom) ice mass density at three early times for case E.

throughout the simulation, even when ambient air is highly supersaturated. The majority of particles lost sublimate during the vortex phase. The other statistics plotted, mean ice radius and total ice mass, both increase throughout the simulation as the deposition of water vapor from entrained ambient air outweighs any loss of particle number.

4.2. Sensitivity of Dynamics

[53] In looking at the results of the various sensitivity cases, we will first examine the effect of the parameters on the dynamics of the contrail, as evidenced by properties of the flight-direction averaged cross section. Although the flow is three-dimensional, properties are quasi-homogeneous in the flight direction, and the averaging allows easier examination of the data. Note that despite model differences, most qualitative trends presented in this section are the same as in previous studies [e.g., *Lewellen and Lewellen, 2001; Unterstrasser and Gierens, 2010a*].

[54] In the following figures, the averaged ice mass density in the contrail is plotted. Examining the ice in the contrail cross-section shows how the ice is distributed by the fluid dynamics of the contrail. The averaged cross-section is shown at two times: $t = 300$ s, at the end of the vortex phase, and $t = 1200$ s, at the end of the simulation. Cases L and M, which reduce the ambient relative humidity from the baseline 130%, and cases E2 and M2, which reduce the effective emission index of ice nuclei from the baseline 10^{15} kg^{-1} , are not shown in this section. For these cases, the dynamical behavior of the contrail is nearly identical to the baseline case E.

[55] Figure 10 shows data from the cases in which aircraft type was varied (cases E, F, and G). At $t = 300$ s, the early

effects of different aircraft types are evident in the vertical extent of the ice. The largest aircraft produces the strongest vortex descent and is spread over the greatest vertical extent. This effect persists to the end of the simulation, where case F also has the greatest vertical extent. The effect on vertical extent will become more important in the presence of shear, as discussed below. The total amount of ice present in the contrail is also clearly the largest for case F and smallest for case G - this will be discussed in looking at the sensitivity of ice content in section 4.3.

[56] Figure 11 shows data from the cases in which atmospheric stability was varied (cases E, E4, and E5). The atmospheric stability has a strong effect on the dynamics of the contrail. As detailed in section 4.1, the primary wake descends and then rebounds because it is buoyant. This vertical oscillation damps out as the contrail reaches an equilibrium position. In the strongly stable case, case E5, the wake descent is smaller, and the overall vertical extent of the resulting contrail is smaller as oscillations damp out quickly. This also results in less horizontal spreading and less ice growth at late times, since damping reduces the turbulent energy inside the contrail and less mixing with ambient air occurs. In the neutrally stable case, the wake descent is larger, as entrained air does not provide additional buoyancy to retard the descent rate. The overall vertical extent of the contrail is larger, because no gradient of potential temperature is present to stabilize the buoyant exhaust after the vortex phase. The contrail rises well above the flight level and continues to rise at the end of the simulation time. This rising plume of buoyant fluid entrains more ambient air than the stable cases and the contrail has a larger cross-sectional

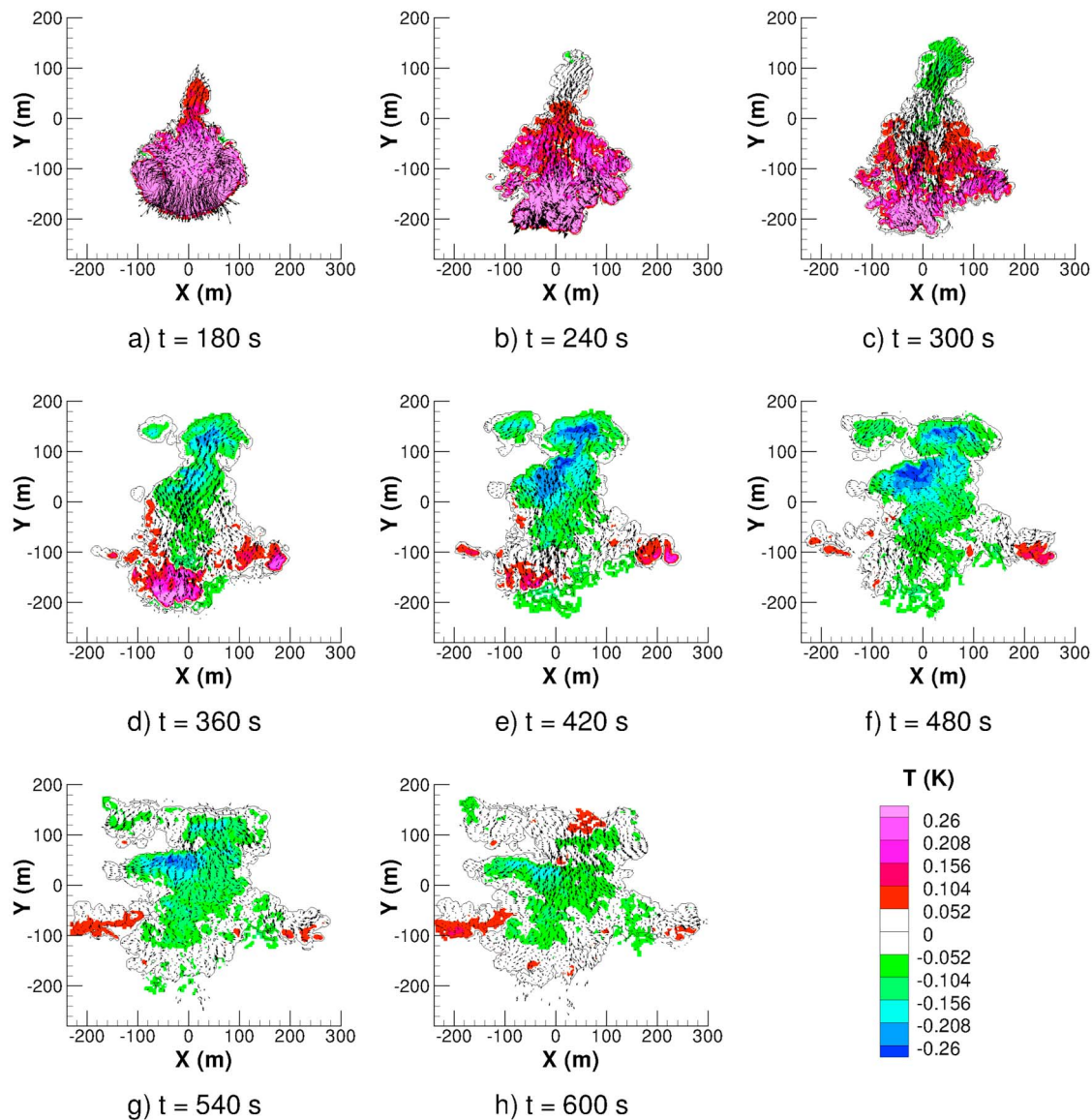


Figure 5. Contours of perturbation potential temperature for a streamwise slice through the center of the vortex-formed downward puff for case E. The line contour shows the outer extent of the exhaust scalar and the vectors show the velocity field tangent to the slice plane.

area. The ice mass density is lower on average, but as shown in section 4.3, the total ice mass is greater due to this increased entrainment.

[57] Figure 12 shows data from the cases in which the aircraft type was varied in the presence of vertical shear (cases C, H). The most dramatic effect of vertical shear is the kinematic spreading of the contrail horizontally. The horizontal extent of these contrails is more than double the extent of the zero shear cases for the respective aircraft types at the end of the simulation. As mentioned above, the effect of aircraft type on contrail extent becomes more important when shear is present. Since the horizontal velocity varies linearly with height, any increase in vertical extent (here, due to increased primary wake descent for the larger aircraft in case H) also increases the horizontal spread of the contrail.

4.3. Sensitivity of Ice Content

[58] The growth of ice in the contrail is also affected by the parameters varied in the sensitivity cases. In this section, we examine domain-integrated ice statistics, specifically percentage of surviving ice particles, mean ice radius, and total ice mass. These quantities provide a simple way of seeing how different variations affect the ice growth and allow further explanation of contrail optical properties in the next section. Again, despite model differences, most qualitative trends in these quantities are the same as in previous studies. One exception is noted below.

[59] Figures 13 and 14 show the ice statistics plotted against simulation time for each of the sensitivity cases, separated by parameter category. Figure 13 (top) shows the variation of results with wind shear for two aircraft types

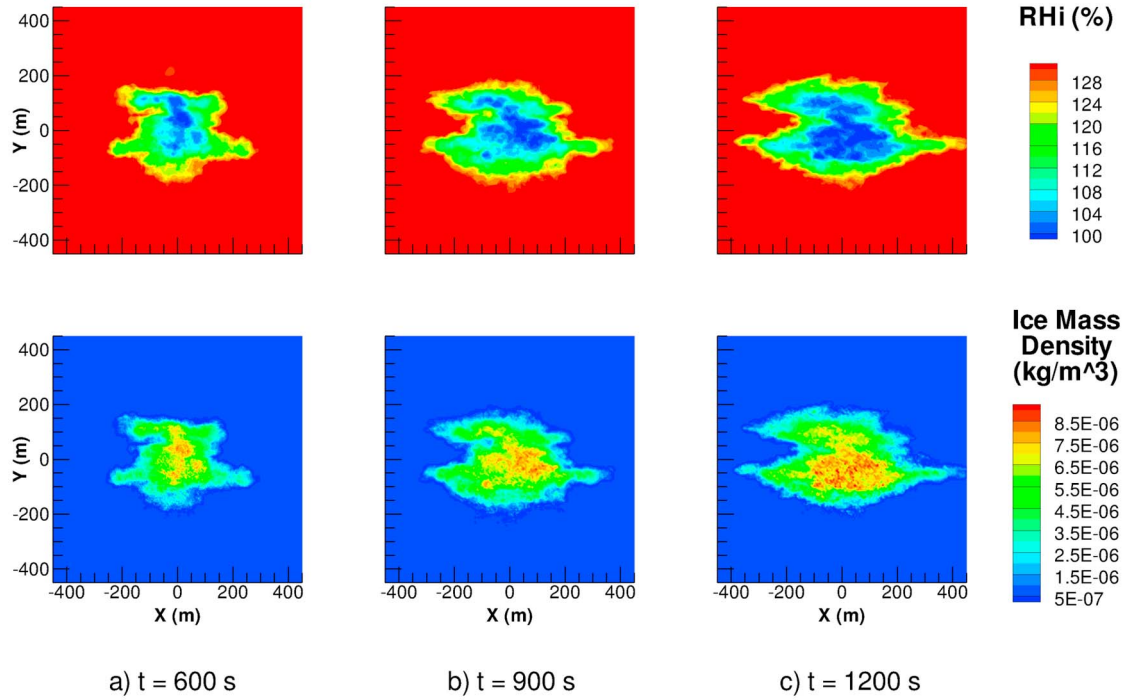


Figure 6. Flight-direction averaged contours of relative humidity with respect to (top) ice and (bottom) ice mass density at three late times for case E.

(cases E, C, F, and H). No significant change in the number of surviving ice particles is caused by the addition of shear. Mean radius is 5% larger in each shear case and total ice mass is 20% larger. As shear spreads the contrail horizontally, its surface area grows, allowing more turbulent mixing of humid ambient air into the contrail at its periphery. This additional mixing provides more water for deposition to contrail ice as the contrail cross-sectional area grows larger.

[60] Figure 13 (middle) shows the variation of results with aircraft type (cases E, F, and G). The percentage of surviving ice particles is related to the descent rate of the vortex wake produced by each aircraft type, which is faster for larger types in these cases. The faster descent warms the primary wake more before the vortices break up, and so a larger fraction of the particles are lost. In absolute terms, the number of particles surviving is still higher for the larger aircraft. Each of these cases produced nearly the same mean

ice radius throughout the simulation, but the total ice mass is roughly proportional to the number of surviving particles, indicating that the distribution of particle sizes is similar for these three cases.

[61] Figure 13 (bottom) shows the variation of results with ambient relative humidity (cases E, L, and M). The number of surviving particles decreases with ambient humidity in the long term. This trend is not as strong as noted in other studies in the literature [e.g., *Unterstrasser et al.*, 2008], and close examination shows that our results show the opposite trend at early times. During the vortex phase, once particles begin to sublimate entirely, the rate of crystal loss is higher for lower ambient humidity, and the lower humidity cases catch up to and surpass the crystal loss in higher ambient humidity cases. This discrepancy may be due to the initial condition used in this study, sensitivity to which has not yet been assessed. It is also possible that insufficient Lagrangian

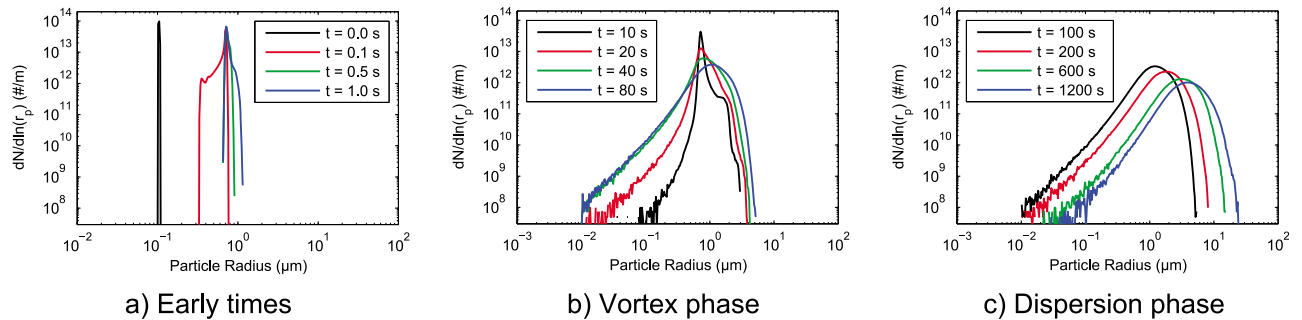


Figure 7. Domain-integrated ice particle size PDFs for case E at a series of times throughout the simulation.

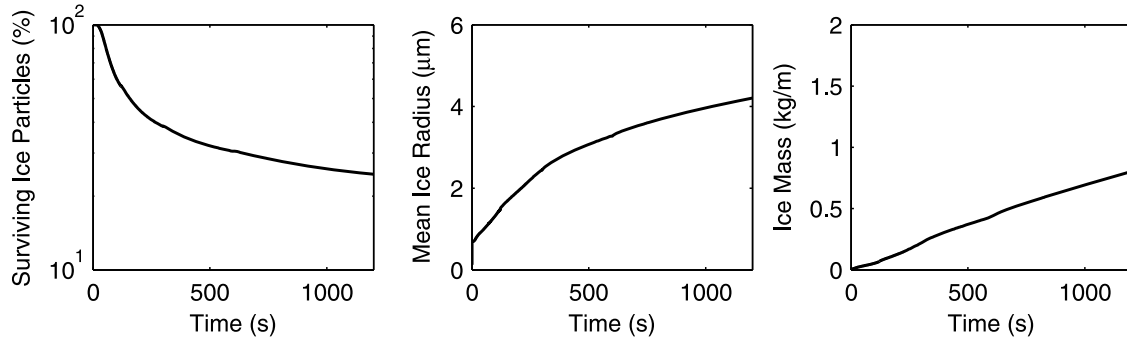


Figure 8. Domain-integrated ice particle statistics plotted against simulation time for case E.

particle resolution leads to errors in the early size distribution of ice, which changes the early time crystal loss rate. As noted in the previous section, the amount of ice deposited to the contrail particles is controlled by the ambient humidity at late times as humid air is entrained in the contrail. This is reflected in the increase of both mean ice radius and total ice mass with increasing humidity in these cases.

[62] Figure 14 (top) shows the variation of results with atmospheric stability (cases E, E4, and E5). No significant change in the number of surviving ice particles occurs for these cases. As noted in the previous section, the ice growth is slower in the strongly stable case due to decreased entrainment of ambient air. The opposite is true for the neutrally stable case. The respectively slower and faster ice growth is reflected in both the mean ice radius and total ice mass for these cases. Note that unlike the sensitivities in the other cases presented here, the differences due to atmospheric stability only appear at late times (the beginning of the dispersion phase), when the ice growth is controlled by entrainment of ambient air due to turbulent mixing of the contrail.

[63] Figure 14 (bottom) shows the variation of results with ice nuclei emission index (EI) for two ambient humidity levels (cases E, E2, M, and M2). For the low EI cases, almost no particles are lost during the vortex phase, unlike the high EI cases. This indicates that in the low EI cases, ice particles are low enough in density that they rarely encounter regions of subsaturation for long enough times to completely sublimate. Although number densities are an order of magnitude lower for the low EI cases, the same amount of water vapor is present as in the high EI cases. Since ice growth is controlled by the degree of supersaturation, approximately the same mass of water must deposit on the contrail ice to reach equilibrium at saturation. Thus, the total ice mass in the domain is the same throughout the simulation for the same ambient humidity in both the low and high EI cases. To make up for the reduced number of particles, mean ice radius is much larger in the low EI cases.

4.4. Sensitivity of Optical Properties

[64] The final comparison of the sensitivity cases will examine the optical properties of the contrails. The optical properties of these clouds can be characterized by their optical depth and their area coverage. In keeping with our flight-direction averaging approach from section 4.2, we will characterize the coverage of a case by the width of its

averaged cross-section. The area covered by a particular contrail could then, in principle, be calculated by multiplying its width by its length in the flight direction.

[65] Contrail optical depth and cross-sectional projected width are derived from the simulation data by post-processing as shown schematically in Figure 15. First, contrail optical extinction, τ , is calculated for each 3D grid cell in the domain,

$$\tau = \sum_{i=1}^N \pi r_i^2 Q_i \frac{N_p}{\Delta V}, \quad (17)$$

where N is the number of computational particles in the grid cell, r_i is radius of each particle, ΔV is the volume of the grid cell, and Q_i is the total single-particle extinction efficiency of each particle. Q is calculated as a function of particle radius using Lorenz-Mie theory for a wavelength of 500 nm, assuming that the absorption efficiency is negligible with a refractive index of ice of $1.3 + 0i$. These values are averaged in the flight direction, then integrated in the vertical direction to produce an optical depth across the width of the contrail. A Gaussian curve is fit to this distribution. As shown in Figure 15, the optical depth reported is the amplitude of the fit Gaussian, while the contrail width reported is 4σ , where σ^2 is the variance of the fit Gaussian.

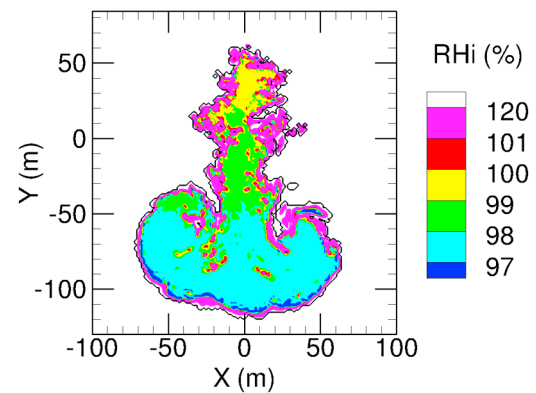


Figure 9. A slice (constant z) through the contrail showing contours of relative humidity at $t = 120$ s for case E. The black line indicates the outer extent of the region containing ice particles.

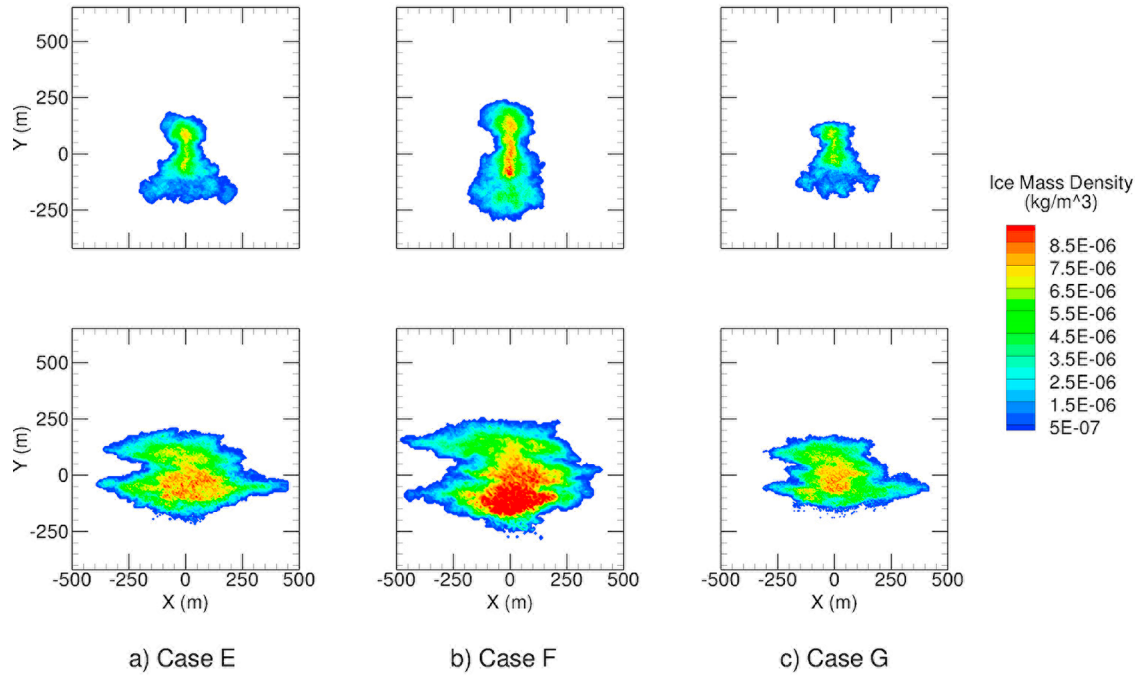


Figure 10. Flight-direction averaged contours of ice mass density showing variations with aircraft type at (top) $t = 300$ s and (bottom) 1200 s. Note that contour levels are the same in each plot. (a) Case E: Medium 2-engine, (b) Case F: Large 4-engine, and (c) Case G: Small 2-engine.

These quantities are only available at discrete times when the relevant data were saved.

[66] Other definitions of optical depth and contrail width are possible and have been used elsewhere. For example,

Unterstrasser and Gierens [2010a] report a predominant contrail optical depth, representing a characteristic or mean value, and a contrail width based on a visibility criterion. We have chosen to report the parameters of a Gaussian fit to

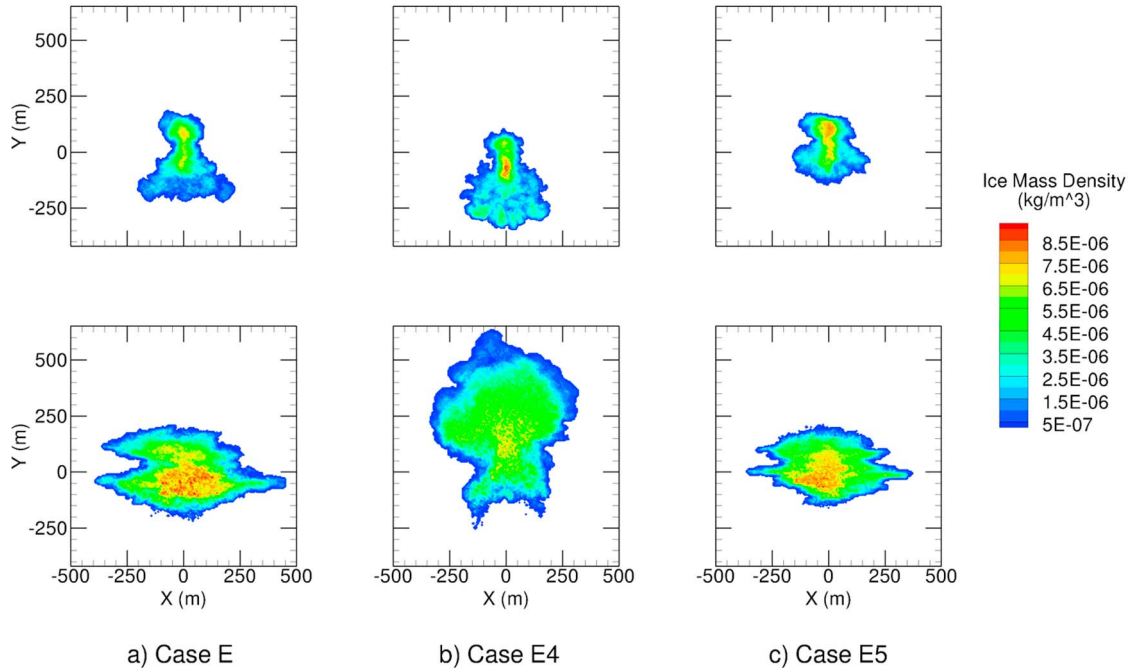


Figure 11. Flight-direction averaged contours of ice mass density showing variations with atmospheric stability at (top) $t = 300$ s and (bottom) 1200 s. Note that contour levels are the same in each plot. (a) Case E: $N_{bv} = 0.01 \text{ s}^{-1}$, (b) Case E4: $N_{bv} = 0.0 \text{ s}^{-1}$, and (c) Case E5: $N_{bv} = 0.015 \text{ s}^{-1}$.

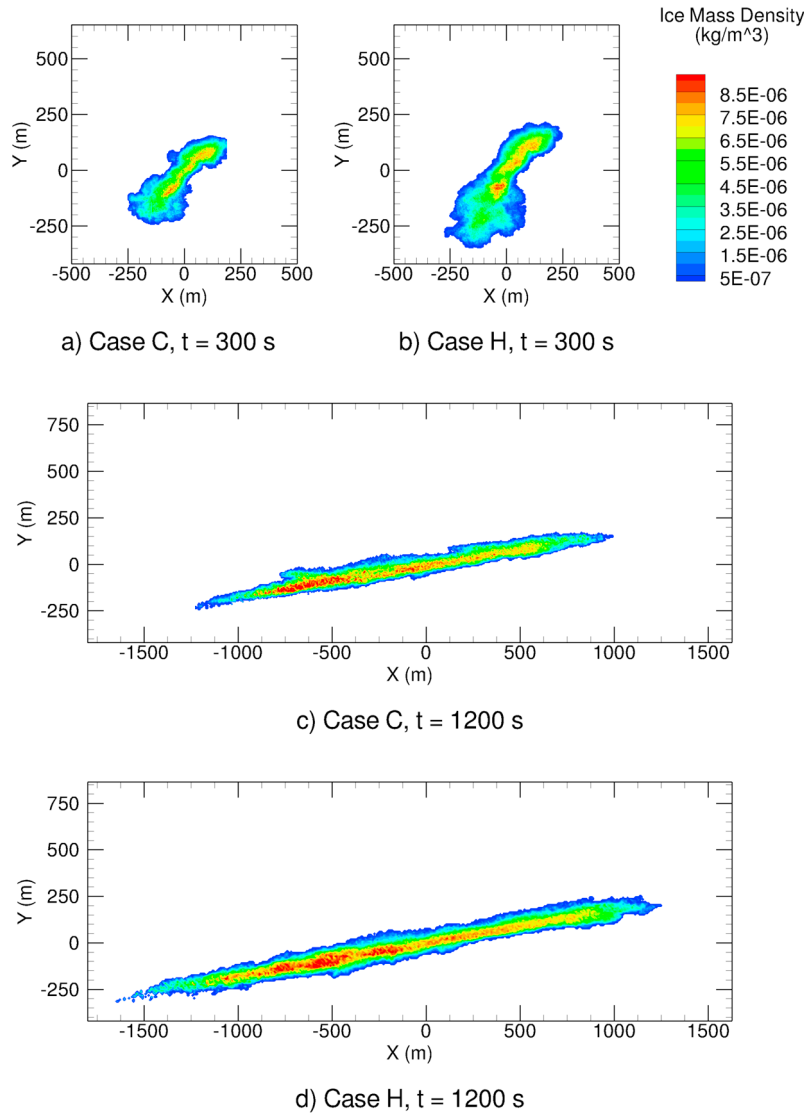


Figure 12. Flight-direction averaged contours of ice mass density showing variations with aircraft type and vertical shear. Note that contour levels are the same in each plot. (a and c) Case C: Medium 2-engine aircraft. (b and d) Case H: Large 4-engine aircraft.

our data because this allows reconstruction of other measures of optical thickness and contrail extent if desired. We found that a Gaussian provided an excellent fit to the optical depth data, especially during the dispersion phase and in the presence of shear.

[67] The behavior of contrail optical depth and width is similar for each case and is worth discussing before sensitivities are addressed. In each case, the optical depth increases through the vortex phase, reaches a maximum, and then decreases through the dispersion phase. Correspondingly, the width decreases slightly through the vortex phase, reaches a minimum, and then increases through the dispersion phase. As shown in section 4.1, during the vortex phase the contrail is tightly bound to the vortices. Ice growth occurs within a relatively constant width region, increasing the ice number density, average radius, and thus optical depth there. As the contrail enters the dispersion phase, this horizontal confinement ends and the spanwise spreading of

the contrail decreases its optical depth while increasing its width. Although width continues to increase throughout the simulation, the entrainment of humid ambient air and subsequent ice growth balances the dilution of the contrail, and optical depth decreases slowly by the end of the simulation.

[68] Figure 16 shows optical depth and projected width plotted against simulation time for each of the sensitivity cases, separated by parameter category. The first row shows the variation of results with wind shear for two aircraft types (cases E, C, F, and H). For each aircraft, no significant differences in optical depth or width appear during the vortex phase. In the dispersion phase, the kinematic effect of shear in spreading the contrail horizontally dominates both the optical depth and the width in the shear cases. As the contrail is sheared, it becomes geometrically shallower and wider (see Figure 12), reducing its optical depth and increasing its width. For case H, shear reduces the optical depth by 79% and increases the width by 450% relative to

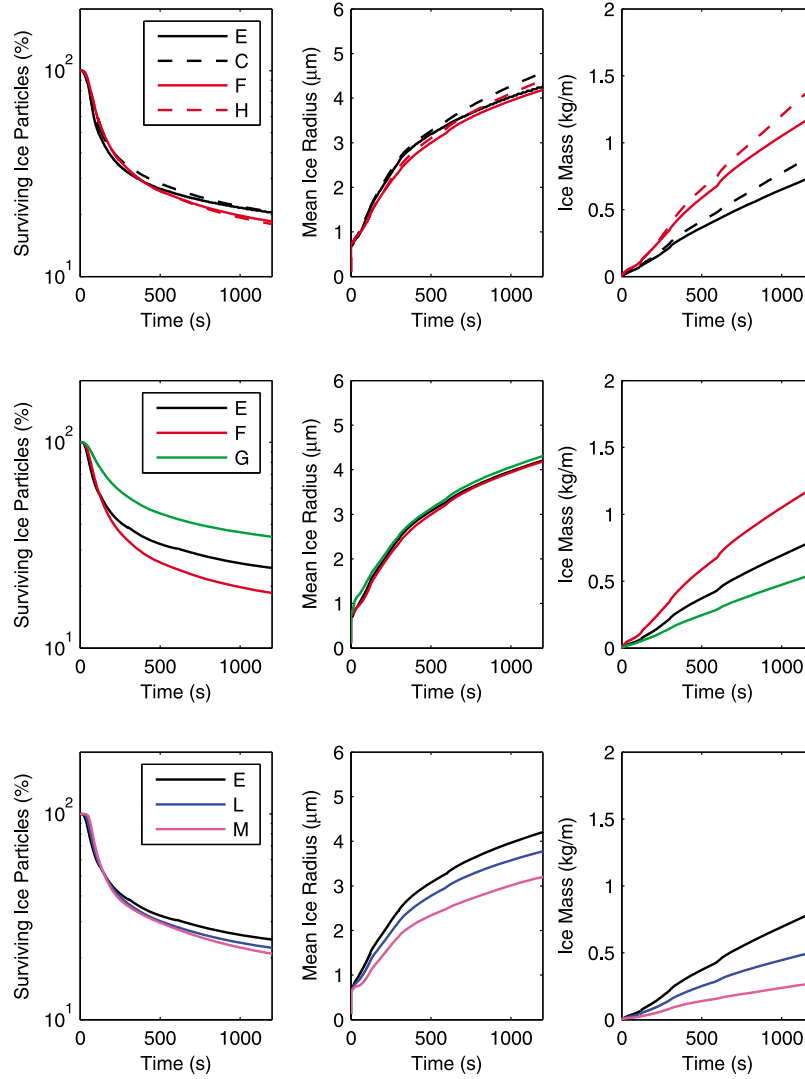


Figure 13. Domain-integrated ice particle statistics plotted against simulation time for the sensitivity cases. Note that linestyles are consistent across all plots.

case F. Similarly, for case C, shear reduces the optical depth by 74% and increases the width by 325% relative to case E. The difference in final width between case C and case H is also notable—the effect of shear has been to spread the contrail of case H, which has a greater vertical extent due to the larger vortex descent, further horizontally.

[69] The second row of Figure 16 shows the variation of results with aircraft type (cases E, F, and G). Optical depth increases with aircraft size. This sensitivity depends on differences in ice properties, rather than on contrail kinematics as in the sheared cases. Optical extinction scales with particle number density and integrated ice surface area as in equation (17) (the extinction efficiency, Q , is also a weak function of radius). More particles are produced by larger aircraft, since they burn more fuel. The volume that these particles are initially dispersed in is larger, however, since it scales with wing span squared. Simple calculation from the values of particle number and wing span listed in Table 4 indicates that the net effect of these parameters is to increase initial number density with aircraft size. The ice statistics shown in Figure 13 also indicate that the integrated

ice surface area increases with aircraft size. Since the number of surviving particles is larger for the larger aircraft, and the mean ice radius is roughly equal between the cases, the integrated ice surface area must be greater. Higher number density and larger integrated ice surface area both lead to increased optical depth for the larger aircraft. The trend in contrail width is small but evident during the vortex phase, when the contrail is tightly bound to the vortex wake, so width scales with wing span. At late times, cases E and F have approximately the same width, while case G is narrower. This emphasizes that ambient turbulence dominates late spreading of the contrail, and differences in the dispersion phase are largely due to specific turbulent realizations of individual simulation cases. The question of whether aircraft type affects contrail properties at late times is one that will be revisited in our conclusions and proposals for future work.

[70] The third row of Figure 16 shows the variation of results with ambient humidity (cases E, L, and M). Optical depth increases with humidity. For these cases, the number density is equal over the simulation time, but higher

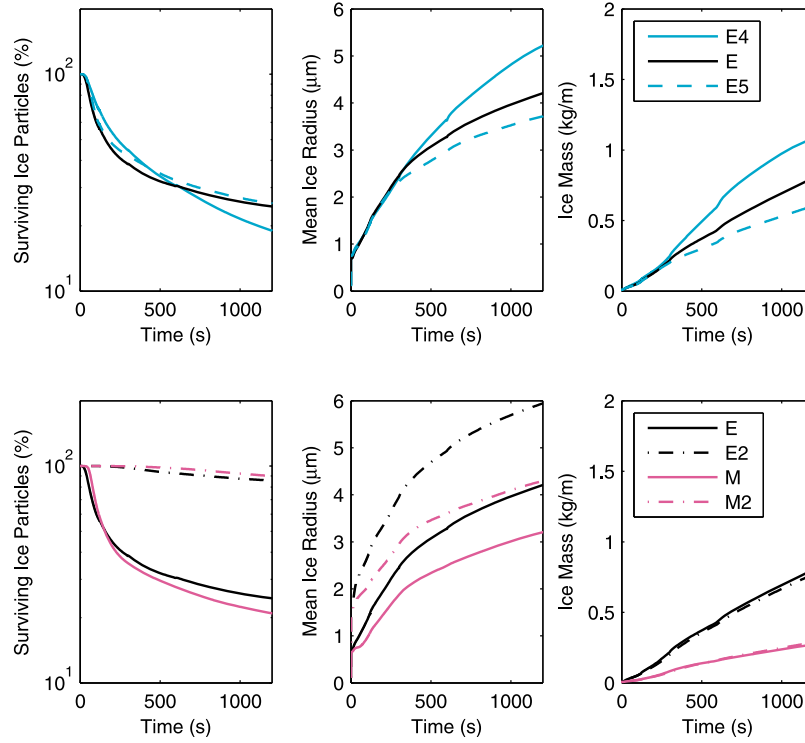


Figure 14. Domain-integrated ice particle statistics plotted against simulation time for the sensitivity cases. Note that linestyles are consistent across all plots.

humidity leads to larger mean particle radius (13). This indicates that integrated ice surface area, and thus optical extinction, is also greater. No significant trend in contrail width appears as humidity is varied, since humidity has little effect on the fluid dynamics. This is a point on which a different metric of width might produce a different conclusion – since contrails for the lower humidity cases are optically thinner, a visibility criterion definition of width might find them to grow smaller or disappear entirely.

[71] The fourth row of Figure 16 shows the variation of results with the emission index of ice nuclei (cases E, E2, M, and M2). For the low EI cases, optical depth is significantly reduced throughout the simulation. This can again be explained by examining the integrated ice statistics (Figure 14). The number of particles present in the low EI cases remains lower than the respective baseline EI cases throughout the simulation. Although the mean ice radius is larger in the low EI cases to keep the mass of deposited ice equal, the increase is not enough to achieve

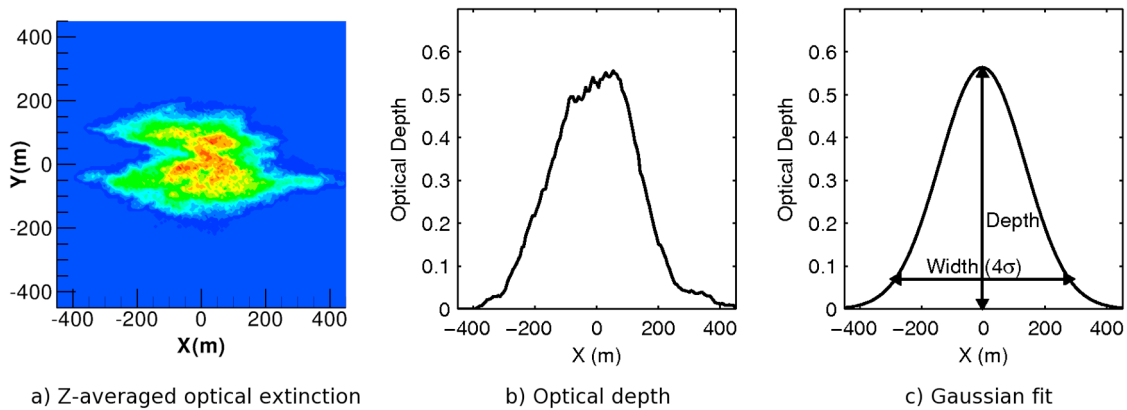


Figure 15. Sequence of the process used to calculate optical depth and contrail width. Ice data from the LES is first used to calculate optical extinction throughout the 3D domain. Optical extinction is then averaged in (a) the flight (z) direction and integrated in the vertical (y) direction to calculate (b) optical depth across the contrail. A (c) Gaussian fits the resulting curve well, especially during the dispersion phase. The data plotted here are for case E at 1200 seconds.

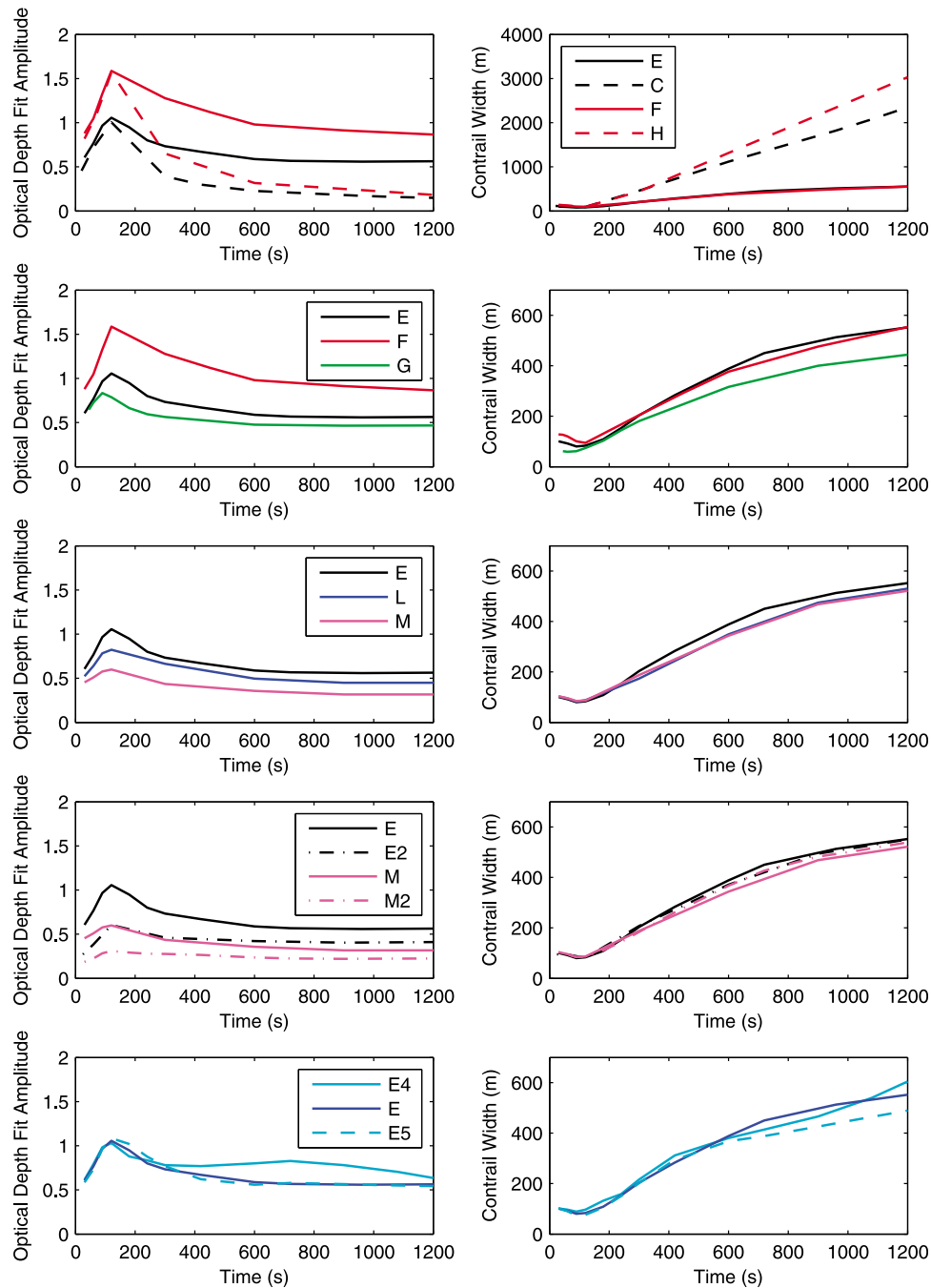


Figure 16. Optical properties plotted against simulation time for the sensitivity cases. Note that line-styles are consistent across all plots.

equal integrated ice area, since mass is a cubic function of radius, while area is only quadratic. No significant trend in contrail width appears as emission index is varied. As in the humidity cases, a different definition of width might produce a different conclusion.

[72] Finally, the fifth row of Figure 16 shows the variation of results with atmospheric stability (cases E, E4, and E5). In the strongly stable case, the optical depth does not change compared to the baseline case, but the contrail width is smaller as expected from the change in the dynamics of this case (section 4.2). The neutrally buoyant case shows a qualitatively different behavior for both optical depth and

width as compared to all of the other cases simulated. During the vortex phase, its optical depth and width are the same as the baseline case. Once the contrail material is released from the vortex wake, the rebound of the buoyant wake is not damped by stability, as noted in section 4.2. The turbulent mixing of the resulting buoyant plume increases the entrainment of humid ambient air. This leads to increased ice growth, which contributes to larger optical depth. As the plume continues to ascend, entrainment also increases the cross-sectional area of the contrail, increasing its width, but also diluting the number density of ice, which reduces the optical depth. The end result of these competing

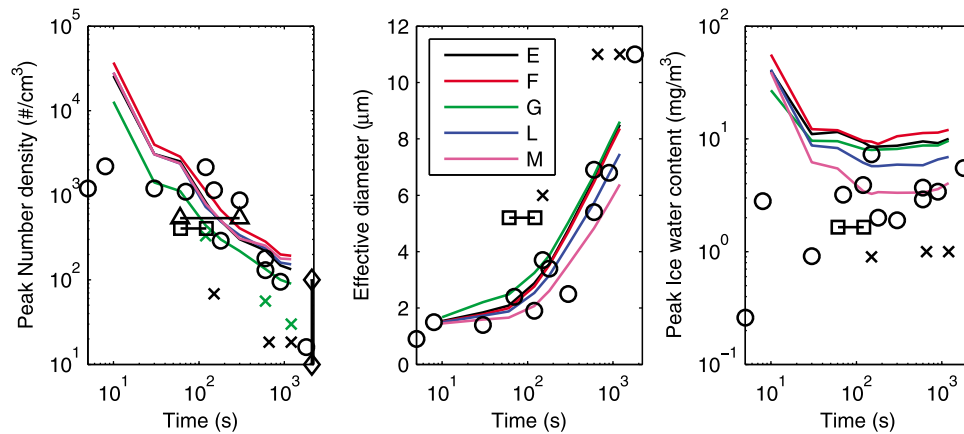


Figure 17. Comparison of LES data (solid lines) to in situ observations (black symbols) of contrail microphysical properties. Circle, *Schröder et al.* [2000]; times sign, *Febvre et al.* [2009]; diamond, *Heymsfield et al.* [1998]; triangle, *Voigt et al.* [2010] A380 aircraft; box, *Voigt et al.* [2010] CRJ-2 aircraft. The green times signs indicate number concentrations derived from the LES data for the small 2-engine case in which only particles with diameter greater than $1 \mu\text{m}$ were considered.

effects is the rise, then fall, of optical depth during the dispersion phase, and also an inflection in the slope of the contrail width as it increases more rapidly at later times.

5. Comparisons to Observations

[73] A limited number of observational studies have been conducted including in situ measurements from aircraft and remote observations from ground and satellite sensors. In this section, we will describe how observational studies of contrails from each study type compare to our simulation results. The simulation cases do not reflect any exact observational conditions, so quantitative comparison must be interpreted carefully.

5.1. In Situ Observations

[74] *Heymsfield et al.* [1998] report in situ microphysical measurements of the contrail behind a NASA DC-8 from the NASA SUCCESS program. *Schröder et al.* [2000] summarize in situ observations from the German SULFUR and AEROCONTRAIL programs that were made from a combination of optical and nonoptical particle detection methods. They report microphysical properties of ice particles for 12 different contrails of ages ranging from 5 s to beyond 30 minutes. *Febvre et al.* [2009] report in situ observations from the German PAZI-2 project for a commercial Embraer-170 contrail that was sampled 2.5 minutes and again between 11 and 20 minutes after the aircraft passed. *Voigt et al.* [2010] report some of the observations from the German CONCERT campaign in which 22 contrails from 11 aircraft types were sampled at ages up to 10 minutes.

[75] We summarize the observed data in Figure 17 along with data from our simulations. Of the data reported by *Heymsfield et al.* [1998], only the number density of particles of diameter 1 to $40 \mu\text{m}$ is of use for comparison. *Schröder et al.* [2000] give measured number density, effective particle diameter, and ice water density at a single age (in some cases, estimated) for each of the contrails observed. *Febvre et al.* [2009] give values for number density, effective particle diameter, and ice water density

(all for particles of diameter $>1 \mu\text{m}$) for a young contrail and the same contrail, “slightly aged” (providing a single value for their measurements between 11 and 20 minutes). *Voigt et al.* [2010] give peak and average measured particle concentrations for two specific contrails, one from an A380 aircraft between 1 and 5 minutes old, and one from a CRJ-2 aircraft between 1 and 2 minutes old. Average measured ice volume concentration and effective radius are also reported for the CRJ-2 contrail.

[76] The sampling location within the contrail is unknown for most of the observations, making comparison with our simulation results difficult. In Figure 17a, we report the maximum number density from the flight-direction averaged field for each of the simulation cases shown. Regions of high number density are also regions of high optical extinction in the contrail, so we surmise that these are also regions most likely to be sampled by pilots attempting to fly through contrails by visual identification. The simulation values thus provide a reasonable upper bound on the expected observations. The values from *Schröder et al.* [2000] appear to match well with simulation results. One observation (their contrail “E”) has an unexpectedly high number density at $t = 5$ minutes, but several of the observations (their contrails “A2”, “B2”, “F”, and “O”) match very well with our small 2-engine aircraft case at later simulation times. As these contrails were produced by relatively small jets (respectively, an Airbus 300, Boeing 737, and Falcon, with the “O” produced by an unknown aircraft), this match is very encouraging. The values from *Febvre et al.* [2009] are much lower than our simulation or the *Schröder et al.* [2000] data. Their analysis was restricted to particles larger than $1 \mu\text{m}$ diameter, however, whereas we report number density of all our particles, of which there are many smaller than this size (see Figure 7 for the size distribution of particles in the simulations). For comparison, we also show LES data from the small 2-engine aircraft case in which only particles with diameter greater than $1 \mu\text{m}$ were considered. These do match the *Febvre et al.* [2009] observations more closely at the end of the simulation. *Febvre et al.* [2009] did also see peaks in number

concentration up to 200 cm^{-3} for the young contrail and up to 130 cm^{-3} for the aged contrail, and these values would bring their observations in line with our study. The peak value seen by Voigt *et al.* [2010] for the A380 agrees well with our simulation data, given the range in age over which the observations occurred. Likewise, the peak value for the CRJ-2 lies just below the simulation result for the small aircraft, following the trend seen in the simulation results of decreasing number density with aircraft size. The values given by Heymsfield *et al.* [1998] were for observations later than the end of our simulations, but extrapolation of our results in time would be near the upper end of their observed range.

[77] For the microphysical properties that depend on atmospheric conditions, there is again difficulty in comparing observational data to our simulation results, since the conditions in which the observations were made are not always closely specified. Schröder *et al.* [2000] report estimated ambient humidity for each of the contrails they observed, but several appear to be subsaturated with respect to ice, which we expect to sharply reduce particle size and ice water density. The contrail observed by Febvre *et al.* [2009] occurred in a supersaturated region. In Figure 17b, we report the mean particle diameter for each of the simulation cases shown, which for our spherical particles is equivalent to the effective diameter reported in the observational studies. Again, the observations of Schröder *et al.* [2000] match very well with our simulation results. The values for effective diameter observed by Febvre *et al.* [2009] are larger. The value observed by Voigt *et al.* [2010] for the CRJ-2 is also larger.

[78] Figure 17c shows the maximum ice water density from the flight-direction averaged field for the simulation results. Again, these represent a reasonable upper bound on the expected observations. The data reported by Schröder *et al.* [2000] falls in or below the results from our simulations. Two of the earlier contrails they observed (contrails “A” and “B”) were evaporating when observed in conditions subsaturated with respect to ice, and these two values are at least an order of magnitude lower than our simulation results. Four of the observed contrails (their contrails “B1”, “B2”, “F”, and “O”) fall right on the curve for our RH_i = 110% case. Contrail “D”, which was observed at a high supersaturation, is between the simulation results for the RH_i = 120% and 130 % cases. The value for contrail “U”, which was from an unidentified aircraft, and for which the humidity was not reported, is also within the extrapolated range of our simulation results. The ice water density observed by Febvre *et al.* [2009] is much smaller than those predicted by our simulations. This observation was for a smaller aircraft than we simulated, however, and as shown in our results, smaller aircraft produce significantly less total ice mass. The combination of low number density, large particle radius, and low ice mass density recorded in the observations also points to the possibility that this contrail was sampled near its periphery. On the edges of the contrail, particles have access to more water (from mixing with humid ambient air), so they grow larger, but are fewer in number and lower in mass density. A similar comparison can be made for the Voigt *et al.* [2010] observations for the CRJ-2 aircraft. For this contrail, Voigt *et al.* [2010] report measured ambient humidity between 82 and 95% with

respect to ice. This slightly subsaturated humidity condition could account for the smaller ice density that they measured.

5.2. Remote-Sensing Observations

[79] Freudenthaler *et al.* [1995] used a ground-based lidar sensor to record cross-sections from many contrails of between 1 and 60 minutes of age. Their study does not report atmospheric or operating conditions for any of the contrails, nor the aircraft that formed them. They aggregated their data into scatterplots showing height, width, and cross-sectional area of contrails plotted against time, where the extent of a contrail was determined by selecting the area just above the maximum background level of the lidar returns. Figure 18 shows a comparison of our LES results to the reported lidar observations, which are represented by the minimum and maximum bounds on the observed data, as well as the line reported by Freudenthaler *et al.* [1995] showing a separation between slowly and quickly growing contrails. The LES results shown are calculated by fitting a two-dimensional Gaussian function to the flight-direction averaged optical extinction fields and using the fit variances to calculate width and area.

[80] LES-derived contrail widths fit well into the slowly and quickly growing contrail categories suggested by Freudenthaler *et al.* [1995]. The quickly growing contrails are those being sheared, while the zero shear cases grow more slowly in width. For growth of contrail area, the LES results also fit well within the range of growth rates observed by Freudenthaler *et al.* [1995], though the separation into categories of slowly and quickly growing is not as clear. We also do not find linear growth of contrail width or area for individual cases, as suggested by Freudenthaler *et al.* [1995], but many of the data points in their plots (that is, for the same contrail) also do not show linear growth in time. A sublinear growth for zero shear cases and super-linear growth for higher shear cases is consistent with other studies of plumes controlled by ambient turbulence [e.g., Dürbeck and Gerz, 1996].

[81] LES-derived contrail widths fit well into the slowly and quickly growing contrail categories suggested by Freudenthaler *et al.* [1995]. The quickly growing contrails are those being sheared, while the zero shear cases grow more slowly in width. For growth of contrail area, the LES results also fit well within the range of growth rates observed by Freudenthaler *et al.* [1995], though the separation into categories of slowly and quickly growing is not as clear. We also do not find linear growth of contrail width or area for individual cases, as suggested by Freudenthaler *et al.* [1995], but many of the data points in their plots (that is, for the same contrail) also do not show linear growth in time. A sublinear growth for zero shear cases and super-linear growth for higher shear cases is consistent with other studies of plumes controlled by ambient turbulence (for example, Dürbeck and Gerz [1996]).

[82] A wide range of visible wavelength optical depths have been measured for contrails - some of the studies reporting these are summarized by Kärcher *et al.* [2009]. Satellite observations are typically only for aged contrails, since young contrails are too small to be resolved by satellite sensors. Duda *et al.* [2004] present satellite observations which they attempted to match to flight tracks from specific commercial flights using coincident meteorological data.

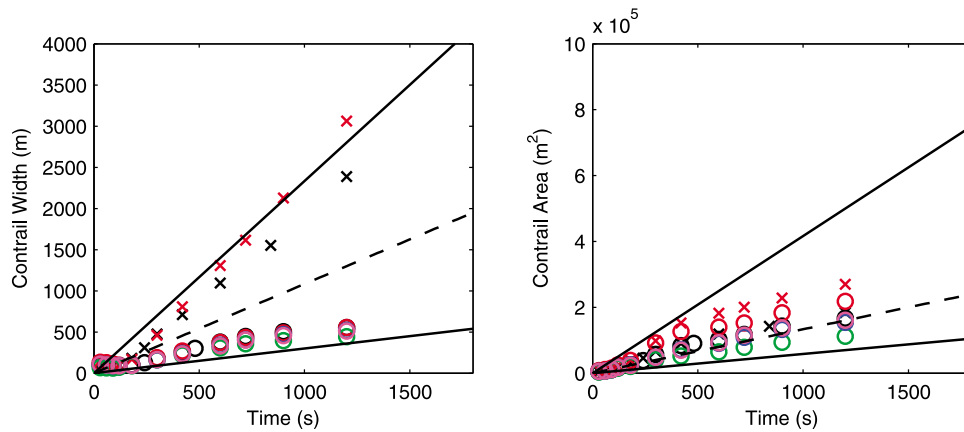


Figure 18. Comparison of LES data (symbols) to the limits of observational data from *Freudenthaler et al.* [1995]. Solid lines denote the minimum and maximum observed contrail widths and areas; dashed lines indicate the separating line between observed slowly and quickly growing contrails. LES data is plotted using colors consistent with the other linestyles in this paper (times sign shows sheared cases, circle shows zero shear cases).

They observed optical depths ranging from 0.1 to 0.6, with the youngest contrails visible in the satellite imagery less than one hour after formation. They also matched contrail formation to conditions that were supersaturated with respect to ice, and made some estimates of other conditions such as vertical wind shear.

[83] The difficulty in comparing such satellite observations to our simulations is a result of low resolution of satellite sensors (1 km at best) and uncertainties in atmospheric conditions and aircraft operating conditions. Since contrails can only be detected once they have spread to a size comparable to the sensor resolution, observations of young contrails is impossible. Still, the contrails at the end of our simulations have optical depths consistent with the ranges observed by satellite. In a more applicable study, *Atlas et al.* [2006] combined ground-based photography with lidar, satellite, and flight track data to calculate optical depths for contrails with fallstreaks ranging between 0.8 and 2.0, with an average value of 0.35 over a 1.5 hour period. Correlation of these contrails to flight tracks indicated that these contrails were approximately 10 minutes to 2 hours of age, which is more comparable to our simulations.

6. Conclusions

[84] In this work, we have presented our simulations of contrail development over twenty minutes of simulation time. Using an LES code with Lagrangian particle tracking has allowed us to model contrail development, including fluid dynamics and microphysics, in three-dimensions with high spatial and temporal resolution. We have also explored a parameter space of potential formation conditions, varying vertical wind shear, aircraft type, ambient relative humidity, ice nuclei emission index, and atmospheric stability. Ice properties, geometric extent, and optical depths of simulated contrails are similar to observational data obtained by in situ measurements, ground-based lidar, and satellites, though direct quantitative comparison is difficult given uncertainties in observational conditions.

[85] Comparison with this observational data highlights the importance of producing reliable data through simulation, since the difficulties in accurately measuring contrail properties in the real world are so great. Simulations allow experimentation with carefully controlled inputs (initial and operating conditions) and produce easily measured outputs (3D data fields), unlike field observations in which neither inputs nor outputs can be easily, accurately, or reliably measured, and for which much expert interpretation is required.

[86] The global simulations that are used to estimate the climate effects of human activities resolve scales much larger than individual contrails. Simple parametric models are thus required to represent contrails when the physics simulated here cannot be resolved. The parameter variations chosen for investigation in this work represent only a small portion of the large parameter space of commercial aircraft flight conditions. Still, the results point toward the parameters on which contrail properties depend most sensitively, and therefore the parameters that should be addressed in models.

[87] For optical depth and contrail width, the strongest sensitivity in the simulations was to vertical wind shear. The quantitative comparisons detailed here are all given for results after twenty minutes of simulation time. For the two cases simulating a large, 4-engine aircraft at 130% RH_i, a moderate vertical wind shear of 0.005 s^{-1} reduced the peak optical depth by 79% as compared to the zero shear case, from 0.87 to 0.18. Shear increased the width by 450% as compared to the zero shear case, from 550 m to 3000 m. Shear caused a similar magnitude reduction of optical depth and increase of width in the medium, 2-engine aircraft cases.

[88] Other parameter variations presented here, aircraft type, ambient humidity, and ice nuclei emission index, had little effect on contrail width in the long term, as ambient turbulence dominated the horizontal spread of the contrails. Optical depth was sensitive to each of these parameters. Under the same 130% RH_i condition, the large, 4-engine

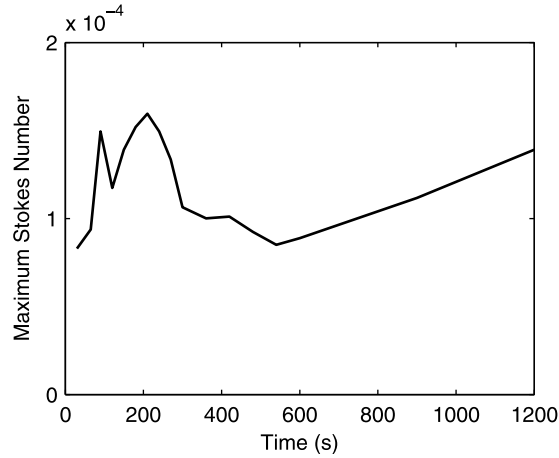


Figure A1. Maximum Stokes number of particles in the simulation plotted against time. The calculation demonstrates that the assumption of small Stokes number is justified in neglecting particle drag forces for this simulation.

aircraft produced a peak optical depth of 0.87, 53% larger than the medium, 2-engine aircraft peak optical depth of 0.56. The small, 2-engine aircraft contrail had a peak optical depth of 0.47, 17% lower than the medium aircraft. For the humidity variations, the 120% and 110% RH_i cases had peak optical depths of 0.45 and 0.32, 20% and 43% lower than the baseline 130% RH_i case respectively. Reducing the ice nuclei emission index by an order of magnitude under 130% and 110% RH_i lowered the peak optical depths to 0.41 and 0.22, 27% and 29% lower than the baseline cases at those humidities respectively. The final variation, in atmospheric stability, gave thinner and narrower contrails for stronger stability and thicker, wider contrails for neutral stability, but only with differences of about 10% from the baseline case.

[89] We note that the quantitative results of our simulations should be used carefully. For example, the specific contrail optical depths and widths reported are for particular cases and their sensitivity to all conditions has not been generally assessed. Also, although the model has been thoroughly tested and validated, questions remain as to whether the current Lagrangian resolution is sufficient to represent ice size distributions throughout the contrail. Differences in the trend in number of surviving particles at early simulation times with ambient humidity between our model and previous studies require further investigation.

[90] This work is intended to support the development and improvement of a global model that calculates the climate impact of aviation [Jacobson *et al.*, 2011]. The climate model uses a parametric sub-grid scale model called the SPM to represent contrail dynamics [Naiman *et al.*, 2010]. The SPM takes grid scale vertical shear and turbulence parameters as inputs and predicts the geometric shape of contrail cross-sections over time. Comparison of sheared LES results with the SPM under the same conditions show that it accurately predicts contrail width as it grows under shear. The LES results presented here thus serve as preliminary validation for the SPM used in climate calculations.

The SPM does not account for other parameters explored here that may have an influence on contrail extent at late times, such as aircraft type and atmospheric stability. It also does not account for sedimentation of ice particles as they grow larger, which may act to spread contrails vertically at late times. The effect of these parameters and processes need to be examined in high fidelity simulations such as LES, where their effect on contrail radiative properties can be properly addressed.

[91] Several additional items of work are therefore planned to improve and extend the simulations presented in this work. The twenty minutes simulated by LES is less than a typical global climate model time step. Full validation of the SPM will require running the LES for several climate model time steps (two or three hours of simulation time). For these longer time runs, several extensions to the LES will be implemented. Large scale turbulence, which is responsible for spreading contrails as they age, will be forced in the fluid dynamics model. A new ice microphysical model will be added to include the effects of sedimentation on ice particle locations, which becomes more important at later times as ice particles continue to grow. The approximation of spherical ice particles also becomes less applicable as the particles grow, and more realistic ice crystal shapes will be included through a model of ice habit. Different ice habits will change both the growth rate of ice and the optical properties of the crystals. The results of these longer time runs will be used to further improve the modeling of contrails within the global model to reduce uncertainties in the magnitude of aviation climate impacts.

Appendix A: Particle Dynamics Validation

[92] In section 2.2, we noted that some of the assumptions made in simplifying the particle dynamics required validation. Figure A1 shows the maximum Stokes number in the simulation domain calculated a posteriori from the case E results. The maximum Stokes number increases early in the simulation, when flow timescales are smaller and ice particles are growing. As the vortex system dissipates, however, fluid velocities in the simulation decay, and the flow time-scale increases. As the dissipation phase continues, particles continue to grow, increasing the maximum Stokes number again. Throughout the twenty minute simulation, the maximum Stokes number remains below 2×10^{-4} .

[93] A more complex model was also implemented to incorporate the effects of inertia, drag, and gravity on particle locations and used in a twenty minute simulation, case K. This provides further validation of the small Stokes number assumption. The equation of motion for a particle is

$$m_p \frac{d\mathbf{v}}{dt} = D(\mathbf{u} - \mathbf{v}) + m_p \mathbf{g}, \quad (\text{A1})$$

where m_p is the particle mass, \mathbf{v} is the particle velocity, and D is the drag force. Drag is approximated using

$$D = \frac{1}{2} \rho c_d A_p |\mathbf{u} - \mathbf{v}|, \quad (\text{A2})$$

where c_d is an empirical function of the particle Reynolds number [Seinfeld and Pandis, 1998] and A_p is the cross-

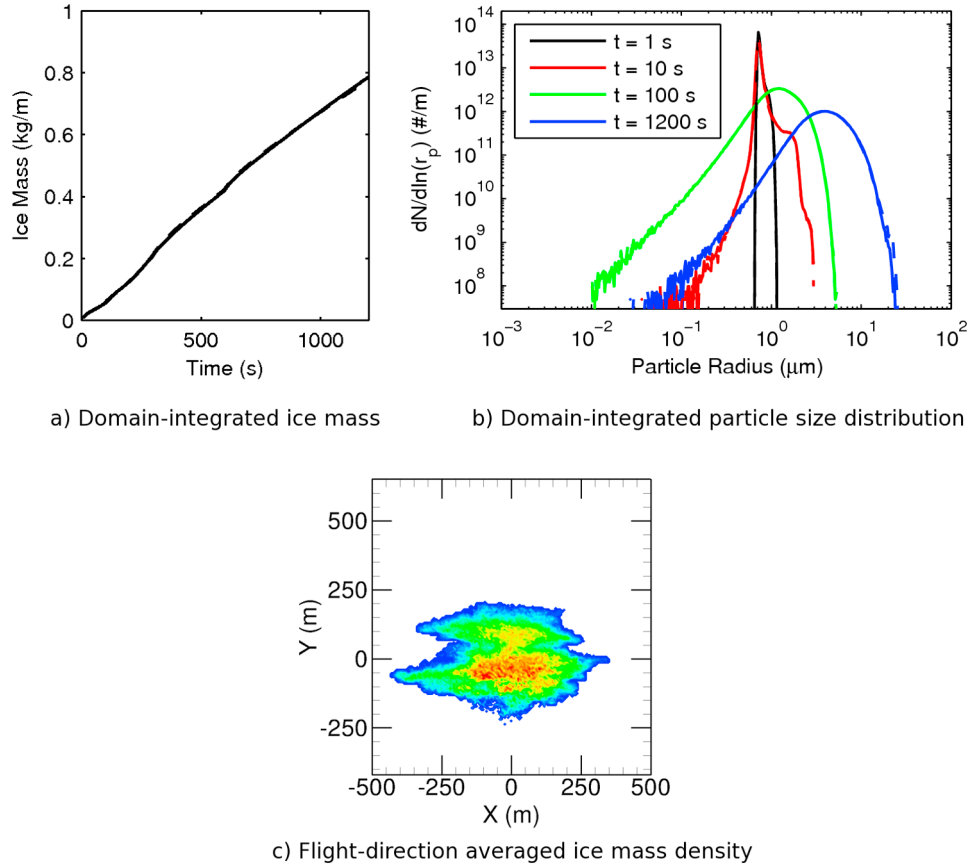


Figure A2. Results from case K, using inertial and sedimenting particles, for comparison with case E. (a and b) The solid line shows data from case E and the dashed line data from case K. (c) Flight-direction averaged ice mass density is plotted at $t = 1200$ s as in Figure 6c, with the same contour levels.

sectional area of the particle. Holding the drag constant over a time step, the particle velocity can be calculated

$$\frac{d\mathbf{x}_p}{dt} = \mathbf{u} - (\mathbf{u} - \mathbf{v}) \exp\left(-\frac{D}{m_p} \Delta t\right) + \frac{m_p \mathbf{g}}{D} \left(1 - \exp\left(-\frac{D}{m_p} \Delta t\right)\right), \quad (\text{A3})$$

where \mathbf{v} is the particle velocity at the beginning of the time step and D is calculated using \mathbf{v} . This replaces equation (8) in the time integration of particle position in case K.

[94] The inertial and sedimenting particles model was used in case K, which was otherwise the same as case E. Some sample results are shown in Figure A2. Ice particle statistics are nearly identical, as shown by both the domain-integrated mass plotted against time and the size distributions at particular times. The averaged ice mass density field has a different distribution due to the particular turbulent realization, but the vertical extent is notably equivalent to that of case E at the same time. It is expected that over longer duration simulations, sedimentation will become more important in spreading the contrail vertically, and the more complex particle dynamics model will be necessary.

[95] **Acknowledgments.** This project is sponsored by the Federal Aviation Administration through the Partnership for AiR Transportation Noise and Emissions Reduction (PARTNER), an FAA-NASA-Transport Canada sponsored Center of Excellence. Any opinions, findings, and con-

clusions or recommendations expressed in this material are those of the authors and do not necessarily reflect the views of the FAA, NASA, or Transport Canada. This research is also supported in part by the National Science Foundation through TeraGrid resources provided by LONI and NCSA under grant TG-CTS080041N. Thanks to our reviewers, whose comments have lead to significant improvement in the paper. Thanks also to S. Baughcum (Boeing), M. Gupta (FAA), R. Halthore (FAA), F. Ham (Stanford), A. Shirgaonkar (MIT), D. Whitt (Stanford), and J. Wilkerson (Stanford).

References

- Atlas, D., Z. Wang, and D. P. Duda (2006), Contrails to cirrus—Morphology, microphysics, and radiative properties, *J. Appl. Meteorol. Climatol.*, **45**, 5–19.
- Chlond, A. (1998), Large-eddy simulation of contrails, *J. Atmos. Sci.*, **55**, 796–819.
- Crow, S. C. (1970), Stability theory for a pair of trailing vortices, *AIAA J.*, **8**, 2172–2179.
- Duda, D. P., P. Minnis, L. Nguyen, and R. Palikonda (2004), A case study of the development of contrail clusters over the great lakes, *J. Atmos. Sci.*, **61**, 1132–1146.
- Dürbeck, T., and T. Gerz (1996), Dispersion of aircraft exhausts in the free atmosphere, *J. Geophys. Res.*, **101**(D20), 26,007–26,015.
- Febvre, G., J.-F. Gayet, A. Minikin, H. Schlager, V. Shcherbakov, O. Jourdan, R. Busen, M. Fiebig, B. Kärcher, and U. Schumann (2009), On optical and microphysical characteristics of contrails and cirrus, *J. Geophys. Res.*, **114**, D02204, doi:10.1029/2008JD010184.
- Forster, P., et al. (2007), Changes in atmospheric constituents and in radiative forcing, in *Climate Change 2007: The Physical Science Basis: Contribution of Working Group I to the Fourth Assessment Report of the IPCC*, edited by S. Solomon et al., Cambridge Univ. Press, New York.

- Freudenthaler, V., F. Homburg, and H. Jäger (1995), Contrail observations by ground-based scanning lidar: Cross-sectional growth, *Geophys. Res. Lett.*, **22**(24), 3501–3504.
- Gerz, T., T. Dürbeck, and P. Konopka (1998), Transport and effective diffusion of aircraft emissions, *J. Geophys. Res.*, **103**(D20), 25,905–25,913.
- Gierens, K. (1996), Numerical simulations of persistent contrails, *J. Atmos. Sci.*, **53**, 3333–3348.
- Gierens, K., and E. Jensen (1998), A numerical study of the contrail-to-cirrus transition, *Geophys. Res. Lett.*, **25**(23), 4341–4344.
- Ham, F., K. Mattsson, G. Iaccarino, and P. Moin (2007), Towards time-stable and accurate LES on unstructured grids, in *Complex Effects in Large Eddy Simulation*, pp. 235–249, Springer, Berlin.
- Heymsfield, A. J., R. P. Lawson, and G. W. Sachse (1998), Growth of ice crystals in a precipitating contrail, *Geophys. Res. Lett.*, **25**(9), 1335–1338.
- Holzäpfel, F., T. Gerz, and R. Baumann (2001), The turbulent decay of trailing vortex pairs in stably stratified environments, *Aerosp. Sci. Technol.*, **5**, 95–108.
- Huebsch, W. W., and D. C. Lewellen (2006), Sensitivity study on contrail evolution, paper AIAA 2006-3749 presented at 36th AIAA Fluid Dynamics Conference and Exhibit, Am. Inst. of Aeronaut. and Astronaut., San Francisco, Calif., 5–8 June.
- Jacobson, M. Z., J. T. Wilkerson, A. D. Naiman, and S. K. Lele (2011), The effects of aircraft on climate and pollution. Part I: Numerical methods for treating the subgrid evolution of discrete size- and composition-resolved contrails from all commercial flights worldwide, *J. Comput. Phys.*, **230**(12), 5115–5132, doi:10.1016/j.jcp.2011.03.031.
- Jensen, E. J., A. S. Ackerman, D. E. Stevens, O. B. Toon, and P. Minnis (1998), Spreading and growth of contrails in a sheared environment, *J. Geophys. Res.*, **103**(D24), 31,557–31,567.
- Kärcher, B., and F. Yu (2009), Role of aircraft soot emissions in contrail formation, *Geophys. Res. Lett.*, **36**, L01804, doi:10.1029/2008GL036649.
- Kärcher, B., T. Peter, U. M. Biermann, and U. Schumann (1996), The initial composition of jet condensation trails, *J. Atmos. Sci.*, **53**, 3066–3083.
- Kärcher, B., U. Burkhardt, S. Unterstrasser, and P. Minnis (2009), Factors controlling contrail cirrus optical depth, *Atmos. Chem. Phys.*, **9**, 6229–6254.
- Lee, D. S., D. W. Fahey, P. M. Forster, P. J. Newton, R. C. N. Wit, L. L. Lim, B. Owen, and R. Sausen (2009), Aviation and global climate change in the 21st century, *Atmos. Environ.*, **43**, 3520–3537.
- Lewellen, D. C., and W. S. Lewellen (2001), The effects of aircraft wake dynamics on contrail development, *J. Atmos. Sci.*, **58**, 390–406.
- Mahesh, K., G. Constantinescu, and P. Moin (2004), A numerical method for large-eddy simulation in complex geometries, *J. Comput. Phys.*, **197**, 215–240, doi:10.1016/j.jcp.2003.11.031.
- Maxey, M. R., and J. J. Riley (1983), Equation of motion for a small rigid sphere in a nonuniform flow, *Phys. Fluids*, **26**, 883–889, doi:10.1063/1.864230.
- Murphy, D. M., and T. Koop (2005), Review of the vapour pressures of ice and supercooled water for atmospheric applications, *Q. J. R. Meteorol. Soc.*, **131**, 1539–1565, doi:10.1256/qj.04.94.
- Naiman, A. (2011), Modeling aircraft contrails and emission plumes for climate impacts, Ph.D. thesis, Stanford Univ., Stanford, Calif.
- Naiman, A. D., S. K. Lele, J. T. Wilkerson, and M. Z. Jacobson (2010), Parameterization of subgrid plume dilution for use in large-scale atmospheric simulations, *Atmos. Chem. Phys.*, **10**, 2551–2560.
- Paoli, R., F. Laporte, and B. Cuenot (2003), Dynamics and mixing in jet/vortex interactions, *Phys. Fluids*, **15**, 1843–1860, doi:10.1063/1.1575232.
- Paoli, R., J. Helie, and T. Poinot (2004), Contrail formation in aircraft wakes, *J. Fluid Mech.*, **502**, 361–373, doi:10.1017/S0022112003007808.
- Paugam, R., R. Paoli, and D. Cariolle (2010), Influence of vortex dynamics and atmospheric turbulence on the early evolution of a contrail, *Atmos. Chem. Phys.*, **10**, 3933–3952.
- Penner, J. E., D. H. Lister, D. J. Griggs, D. J. Dokken, and M. McFarland (Eds.) (1999), *Aviation and the Global Atmosphere*, 373 pp., Cambridge Univ. Press, New York.
- Pozorski, J., and S. V. Apte (2009), Filtered particle tracking in isotropic turbulence and stochastic modeling of subgrid-scale dispersion, *Int. J. Multiphase Flow*, **35**, 118–128.
- Rogallo, R. S. (1981), Numerical experiments in homogeneous turbulence, *Tech. Rep. NASA-TM-81315*, NASA Ames Res. Cent., Mountain View, Calif.
- Schröder, F., B. Kärcher, C. Duroure, J. Ström, A. Petzold, J. F. Gayet, B. Strauss, P. Wendling, and S. Borrmann (2000), On the transition of contrails into cirrus clouds, *J. Atmos. Sci.*, **57**, 464–480.
- Schumann, U. (1996), On conditions for contrail formation from aircraft exhausts, *Meteorol. Z.*, **5**(1), 4–23.
- Schumann, U. (2005), Formation, properties, and climatic effects of contrails, *C. R. Phys.*, **6**, 549–565.
- Seinfeld, J. H., and S. N. Pandis (1998), *Atmospheric Chemistry and Physics: From Air Pollution to Climate Change*, John Wiley, New York.
- Shirgaonkar, A. A., and S. K. Lele (2007), Large eddy simulation of early stage aircraft contrails, *Tech. Rep. TF-100*, Flow Phys. and Comput. Eng. Group, Dep. of Mech. Eng., Stanford Univ. Stanford, Calif.
- Shotorban, B., and F. Mashayek (2006), A stochastic model for particle motion in large-eddy simulation, *J. Turbul.*, **7**(18), doi:10.1080/14685240600595685.
- Spichtinger, P., and K. M. Gierens (2009), Modelling of cirrus clouds—Part 1a: Model description and validation, *Atmos. Chem. Phys.*, **9**, 685–706.
- Spiegel, E. A., and G. Veronis (1960), On the Boussinesq approximation for a compressible fluid, *Astrophys. J.*, **131**, 442–447.
- Unterstrasser, S., and K. Gierens (2010a), Numerical simulations of contrail-to-cirrus transition—Part 1: An extensive parametric study, *Atmos. Chem. Phys.*, **10**, 2017–2036.
- Unterstrasser, S., and K. Gierens (2010b), Numerical simulations of contrail-to-cirrus transition—Part 2: Impact of initial ice crystal number, radiation, stratification, secondary nucleation and layer depth, *Atmos. Chem. Phys.*, **10**, 2037–2051.
- Unterstrasser, S., and I. Sölch (2010), Study of contrail microphysics in the vortex phase with a lagrangian particle tracking model, *Atmos. Chem. Phys.*, **10**, 10,003–10,015, doi:10.5194/acp-10-10003-2010.
- Unterstrasser, S., K. Gierens, and P. Spichtinger (2008), The evolution of contrail microphysics in the vortex phase, *Meteorol. Z.*, **17**(2), 145–156, doi:10.1127/0941-2948/2008/0273.
- Voigt, C., et al. (2010), In-situ observations of young contrails—Overview and selected results from the CONCERT campaign, *Atmos. Chem. Phys.*, **10**, 9039–9056, doi:10.5194/acp-10-9039-2010.
- Wilkerson, J. T., M. Z. Jacobson, A. Malwitz, S. Balasubramanian, R. Wayson, G. Fleming, A. D. Naiman, and S. K. Lele (2010), Analysis of emission data from global commercial aviation: 2004 and 2006, *Atmos. Chem. Phys.*, **10**, 6391–6408, doi:10.5194/acp-10-6391-2010.

M. Z. Jacobson, Department of Civil and Environmental Engineering, Stanford University, Y2E2 Building, 473 Via Ortega, Stanford, CA 94305, USA.

S. K. Lele and A. D. Naiman, Department of Aeronautics and Astronautics, Stanford University, Durand Building, 496 Lomita Mall, Stanford, CA 94305, USA. (anaiman@stanford.edu)